9 Ground-penetrating radar

While seismic-reflection and -refraction techniques are commonly employed to map near-surface layers, they do not have the high vertical resolution (detection of subsurface structures with length scales of 1.0 m or less) that is required for many applications. Ground-penetrating radar (GPR) can be a suitable geophysical tool in these situations. The technique is used to detect changes in subsurface electromagnetic impedance via the propagation and reflection at impedance boundaries of an electromagnetic wave generated by a transmitter deployed at the surface or, less commonly, within a borehole. Typical GPR frequencies are in the 10 MHz to 1 GHz range, much higher than the frequencies used in the electromagnetic (EM) induction method (see Chapter 8). The popularity of GPR as a near-surface geophysical technique lies partially in the similar appearance of radar sections to the seismic sections that are familiar to many geophysicists (Figure 9.1). Both seismic reflection and GPR are imaging techniques based on wave-propagation principles but there are important differences; some of which will be discussed in this chapter. Good overviews of the theory and practice of GPR appear in Davis and Annan (1989), Knight (2001), Neal (2004), Annan (2009), and Conyers (2011).

Example. Perchlorate transport in karst.

The occurrence of the perchlorate ion ClO_4^- in groundwater presents a great risk to human health since perchlorate has long been known to inhibit proper functioning of the thyroid. Beneath the Naval Weapons Industrial Reserve Plant (NWIRP) in central Texas, significant concentrations of perchlorate ions derived from the manufacture of rocket propellant have been detected in groundwater and springs. Hughes (2009) has described a wide-area (~ 500 ha) GPR survey in karst terrain with the goal of mapping subsurface structural features that might be indicative of major pathways for subsurface transport of perchlorate ions. The survey was executed by towing a 50 MHz GPR system for ~ 100 line-km on a sled behind an all-terrain vehicle. The geology consists of a weathered limestone bedrock below a 0–3-m clay overburden. The lateral resolution of the GPR, about 1 m, is far too coarse to detect individual bedrock fractures on the order of millimeters in width. The geophysical targets were therefore identified as top-of-bedrock irregularities, such as weathered downcuts of 1–10 m in width and tens of meters in length, that can be spatially associated with the north-northeast-trending regional structure.

A typical GPR profile from the wide-area survey is shown in Figure 9.2a. On the left side of the profile, the main return signal seen at 20–40 ns is interpreted as a reflection from the top of bedrock at 1–2 m beneath the surface. The bedrock signal is lost at the right side

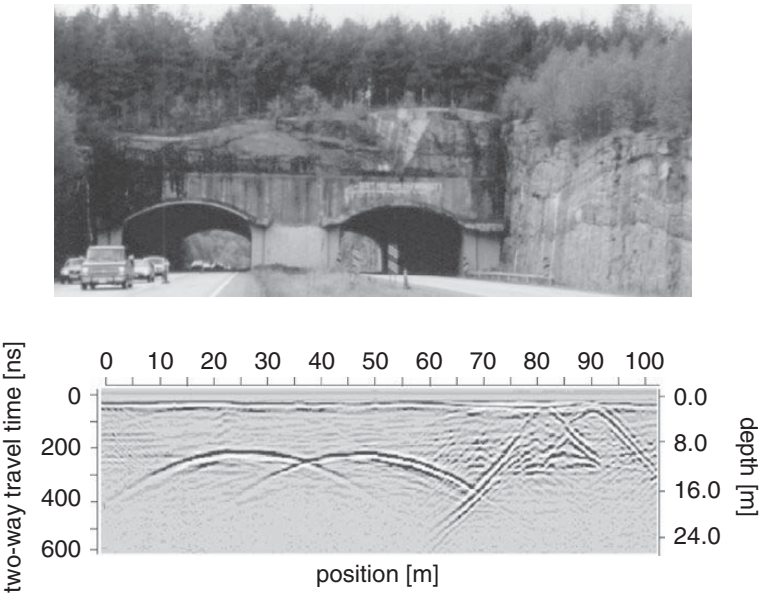

Figure 9.1 GPR section obtained with 50 MHz antennas showing reflection hyperbolas from two road tunnels. The two smaller hyperbolas at the right are caused by scattering from shallow buried objects. After Annan and Davis (1997).

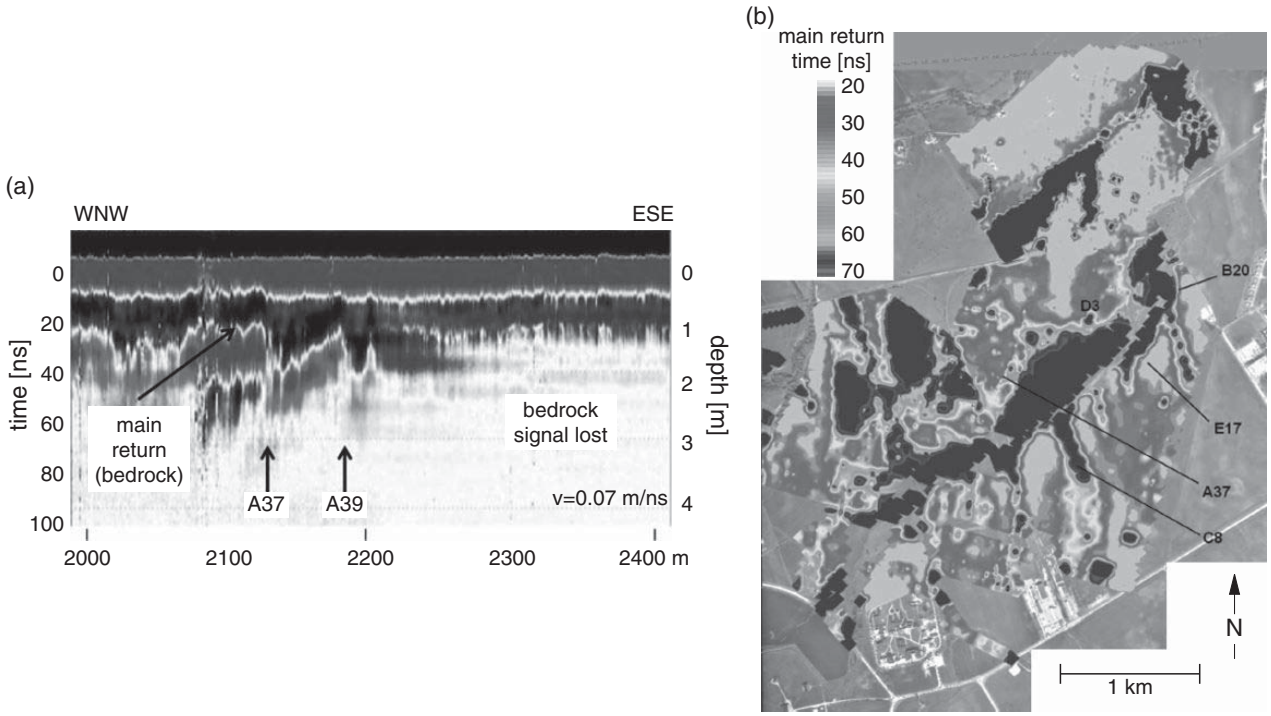

Figure 9.2 (a) Typical GPR section obtained at the NWIRP site, Texas, using 50 MHz antennas; (b) plan-view map of the GPR main returns, interpreted in terms of depth to bedrock. After Hughes (2009).

of the profile due to signal attenuation within a deeper clay overburden. The features marked A37 and A39 are interpreted as bedrock lateral discontinuities. A plan-view map of the two-way traveltime to the GPR main return, assembled from all the GPR profiles in the survey area, is shown in Figure 9.2b. This map can be interpreted as a map of depth to

bedrock, with the magenta regions corresponding to bedrock highs and the blue regions corresponding to bedrock lows. Notice that the dominant orientation of the GPR-inferred bedrock depth map correlates well with the north-northeast geological structural trend. This lends support to the supposition that GPR can provide valuable information about structural controls on subsurface contaminant transport.

Example. Plastic landmine detection.

Landmines and other explosive remnants of war constitute an enduring and severe environmental hazard in dozens of countries that have previously experienced military conflict. Many landmines are now manufactured that contain little or no metal so that metal detectors, long the primary geophysical tool used by humanitarian deminers, often become ineffective. Alternative geophysical techniques, or combinations of techniques, are currently under intense investigation by various commercial, governmental, and non-profit research organizations around the world. The interested reader is invited to explore the United Nations website www.mineaction.org for further information about all aspects of humanitarian demining.

Metwaly (2007) describes GPR imaging results from a 2.5-m $\times$ 6.0-m test site in which five plastic cylinders (Figure 9.3) of similar dimensions (nominal radius 4–5 cm; nominal height 7–13 cm) and construction to anti-personnel landmines were buried up to 22 cm depth in a prepared bed of homogeneous dry sand. It is easy to see from the reflection hyperbolas in the GPR sections that the highest frequency (1.5 GHz) affords the best spatial resolution of the buried objects. The objects labeled 1 and 5 are not well imaged, especially at the lowest frequency, 400 MHz. It may be concluded from this and other studies that plastic, nonmetallic landmines may be identified using GPR techniques provided the following conditions hold: (a) there is a sufficiently strong dielectric contrast between the landmine and the host soil; (b) the signal is not overwhelmed by cultural noise (clutter) or shallow subsurface heterogeneities; and (c) the soil electrical conductivity is low, as would likely be the case, for example, in a dry, coarse-grained sedimentary environment with low organic content.

9.1 Fundamentals

In the frequency range 10 MHz $< f <$ 2 GHz, electromagnetic wave propagation in nonmagnetic, resistive Earth materials ($\sigma < 0.01$ S/m) is controlled largely by spatial variations of dielectric permittivity ε in the subsurface. Bound-charge displacement, or *polarization*, is the dominant mechanism although the quasi-free charge migration, or *conduction*, that governs the EM induction technique plays an important role in GPR signal attenuation.

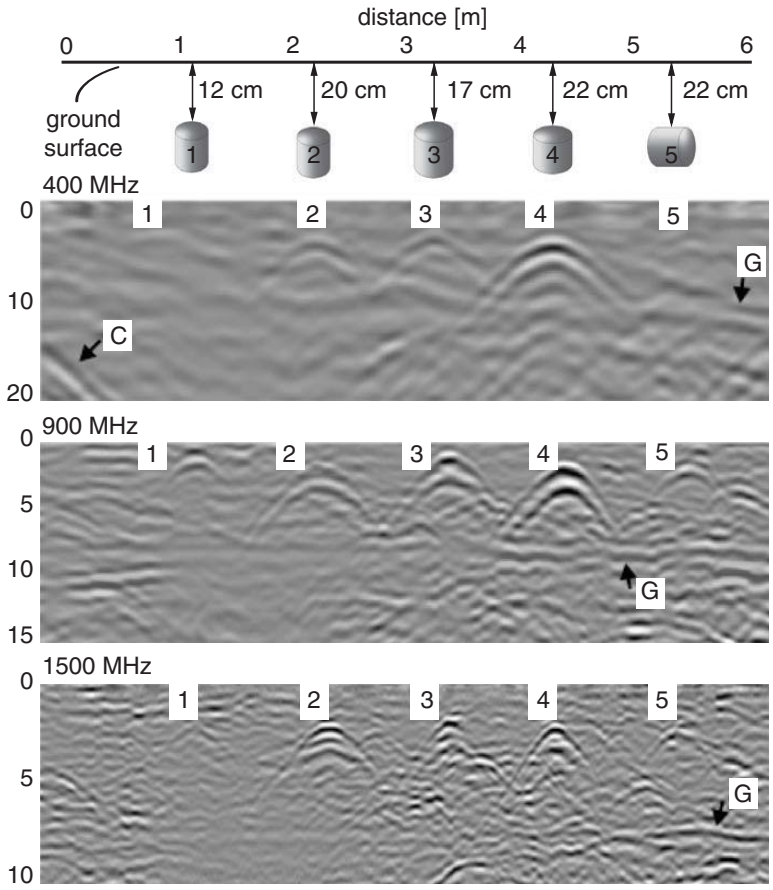

Figure 9.3 GPR detection at three frequencies of plastic-landmine-simulating cylinders buried in homogeneous sand at test site in Egypt; C = unwanted diffraction from an off-site metal sheet; G = reflection from the base of the sand layer; vertical axis is traveltime [ns]. After Metwaly (2007).

The following discussion provides an elementary introduction to the phenomena of atomic, molecular, and interfacial polarization as they are relevant to GPR. Consider an isolated atom consisting of a nucleus of positive charge $+Z$ surrounded by a neutralizing electron atmosphere of charge $-Z$. An applied electric field **E** exerts a force on the electron atmosphere and displaces its charge center, as shown in Figure 9.4a. In essence, the circular orbits of electrons become elliptical (von Hippel, 1954). Similarly, in the presence of an applied field **E**, a polar water molecule will experience a torque which tends to align its *asymmetric* charge distribution into the direction of the applied field, as shown in Figure 9.4b. There is often a small "dielectric loss" caused by some energy that dissipates as the polar molecule rotates, since water is a viscous solvent. The loss term can often be neglected to first order. A non-polar molecule, such as the oxygen molecule O_2, does not exhibit molecular polarization due to its more symmetric distribution of positive and negative charges.

In the GPR frequency range, it is the molecular polarization of the water molecule that largely controls the velocity, and hence the reflection, diffraction, scattering, and other aspects of the subsurface propagation of electromagnetic waves. Atomic polarization does not become an important source of polarization until very high frequencies, greater than

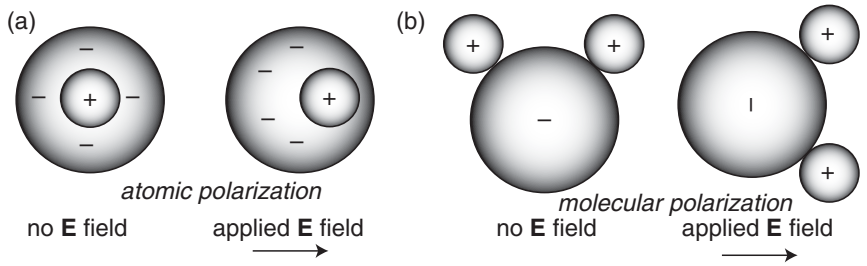

Figure 9.4 (a) Atomic polarization; (b) polarization of the water molecule.

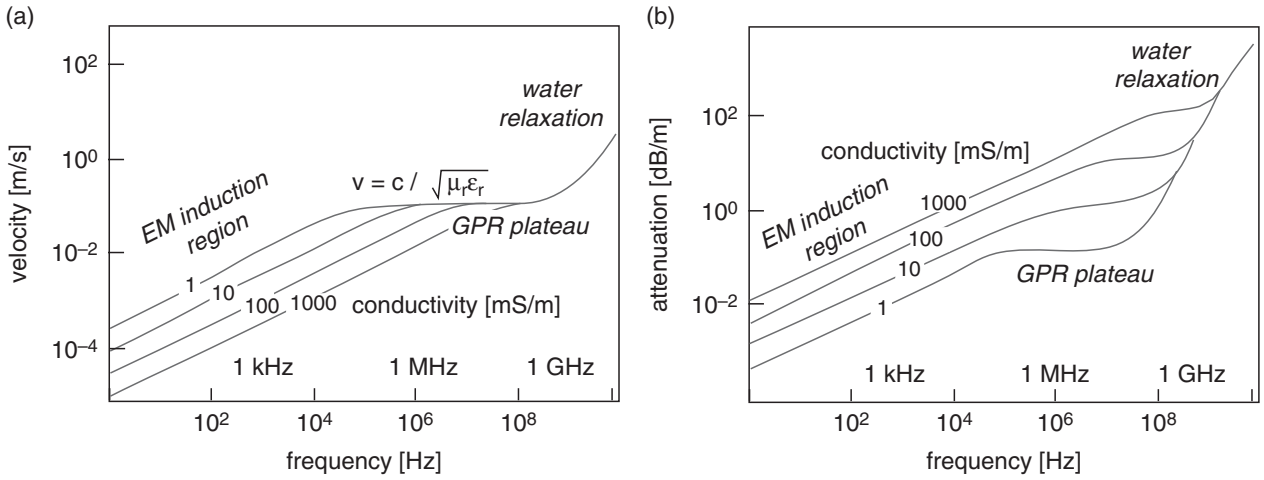

Figure 9.5 (a) GPR wave velocity as a function of frequency; (b) GPR attenuation as a function of frequency. After Davis and Annan (1989).

10 GHz, which is above the normal GPR range. A third type of dielectric polarization, interfacial polarization or the *Maxwell–Wagner effect*, can become important at frequencies less than 100 MHz (Hizem *et al*. 2008). Interfacial polarization at GPR frequencies is caused by electric charges that accumulate at dielectric interfaces when a heterogeneous medium is subjected to an applied electric field.

The electromagnetic wave velocity in a non-magnetic ($\mu_r = 1$) medium is given by the formula (Davis and Annan, 1989)

$$v = \frac{c}{\sqrt{\varepsilon_r}}; \tag{9.1}$$

where $c = 3 \times 10^8$ m/s (~ 1 ft/ns) is the speed of light in vacuum and $\varepsilon_r = \varepsilon/\varepsilon_0$ is the relative electrical permittivity, or *dielectric constant*. Sometimes the symbol K is also used for dielectric constant. To first order, in the radar frequency range 10 MHz– 2 GHz, the velocity v is independent of both frequency and conductivity. This is evidenced by the "GPR plateau" shown in Figure 9.5a.

For most dry geological materials, such as sand, gravel, and crystalline rock, the dielectric constant varies roughly between $3 \leq \varepsilon_r \leq 8$. Water has an anomalously large dielectric constant of $\varepsilon_r \sim 81$ due to the high polarizability of the water molecule in the

Table 9.1 Dielectric constant and radar attenuation of common geological materials at 100 MHz, after Davis and Annan (1989)

Material	Dielectric constant	Attenuation [dB/m]
Air	1	0
Freshwater	80	0.1
Seawater	80	1000
Dry sand	3–5	0.01
Saturated sand	20–30	0.03–0.3
Limestone	4–8	0.4–1.0
Clay	5–40	1–300
Granite	4–6	0.01–1.0

presence of an applied electric field. Thus, water-bearing rocks have significantly higher dielectric constants ($\varepsilon_r \sim 10$–30) than dry rocks of the same lithology. Hydrocarbons such as oil and natural gas have low values of dielectric constants, on the order $\varepsilon_r \sim 1$–2. The dielectric constant and radar attenuation (discussed below) of common geomaterials at 100 MHz is listed in Table 9.1.

The dielectric properties of rocks and soil are generally dispersive at GPR frequencies (West *et al*., 2003), which implies that permittivity ε is a complex function of frequency, often written as $\varepsilon^*(\omega)$. A primary cause of the dispersion is that, at sufficiently high frequencies, the polarization of atoms and molecules cannot keep pace with the rapid alternations of an applied **E** field. This leads to an out-of-phase component of the polarization that manifests itself as an imaginary, or quadrature, contribution to $\varepsilon^*(\omega)$. Moreover, any dielectric loss caused by viscous dissipation of energy as the water molecules rotate in a rapidly changing **E** field adds to the quadrature part of $\varepsilon^*(\omega)$. At frequencies greater than $\sim 10^{10}$ Hz, well above the GPR frequency range, both the real and imaginary components of permittivity $\varepsilon^*(\omega)$ drop precipitously since water molecules are not capable of responding to such extremely fast fluctuations in the **E** field.

The *attenuation* of a radar wave is given approximately by the formula

$$\alpha \sim 1690 \frac{\sigma}{\sqrt{\varepsilon_r}} \quad [\mathrm{dB/m}]. \tag{9.2}$$

A more general, frequency-dependent formula for attenuation α that accounts for both conduction and various forms of dielectric loss is presented in Davis and Annan (1989). As shown in Figure 9.5b, attenuation increases with increasing conductivity σ and frequency ω. This accords with the familiar rule that the GPR depth of penetration decreases as the product $\sigma\omega$ increases. Under poor conditions such as wet, clay-rich soils the penetration depth at ~ 100 MHz is roughly 1–2 m. Under better conditions such as dry, clean sands or gravel, the penetration depth at this frequency can be greater than 10–20 m. In pure rock salt, a low-loss ionic solid, penetration depth can be several hundreds of meters (Gorham *et al*. 2002). The occurrence of fine interbedding restricts the penetration depth of radar

waves as energy is lost at each reflecting horizon. The seismic and GPR techniques are somewhat complementary in the sense that poor GPR field conditions (wet clays) are actually good seismic conditions while ideal GPR conditions (dry sands) are unfavorable for the acquisition of high-quality seismic data.

Geophysical imaging using the GPR method is based on the reflectivity of the geological medium under investigation. Suppose a radar pulse is propagated into a non-magnetic ground which consists of a single layer of dielectric constant ε_1 overlying a halfspace of dielectric constant ε_2. The reflection coefficient for a *normally incident* radar plane wave is

$$R = \frac{\sqrt{\varepsilon_1} - \sqrt{\varepsilon_2}}{\sqrt{\varepsilon_1} + \sqrt{\varepsilon_2}}. \tag{9.3}$$

The reflected energy is proportional to R^2. The general case of oblique incidence of a plane wave will be examined later in this chapter.

9.2 Dielectric constant and electrical conductivity

The velocity of a subsurface radar wave depends on the dielectric constant ε_r, as indicated by Equation (9.1). Radar waves reflect off discontinuities, and bend when they encounter spatial gradients in the local dielectric value. Radar waves are attenuated mainly by electrical conductivity σ. Since the two properties (σ, ε_r) affect radar wave propagation in different ways, it is instructive to examine more closely the relationship between them. This will result in a better understanding of the information content of GPR data.

As a conceptual model, following the discussion in von Hippel (1954), consider two oppositely charged parallel-plate conductors like those shown in Figure 9.6a. The parallel plates of area A and separation d serve as a basic model for a capacitor, which is essentially a charge-storage device. The intervening space is filled with vacuum, so that no electrical current can flow between the plates and accordingly they do not discharge. A voltage V is

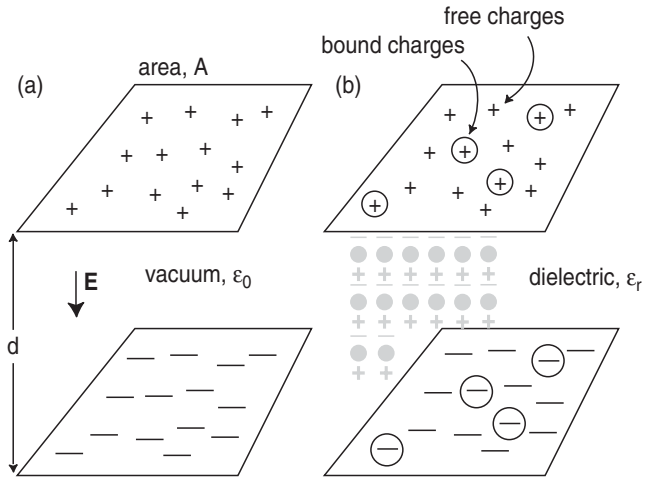

Figure 9.6 A parallel-plate capacitor filled with (a) air; (b) dielectric material.

maintained across the plates by an external battery such that an electric field **E** exists in the $\hat{\mathbf{z}}$ direction, positive downward, as shown.

Let the surface charge density on the two plates be given by $\pm s$ [C/m^2] and the total charge on the plates by $\pm Q$ [C], where $Q = sA$. Now, suppose the space between the plates becomes filled with a dielectric material of relative permittivity ε_r, and zero conductivity $\sigma = 0$, as shown in Figure 9.6b. The electric field **E** now polarizes the dielectric material so that microscopic dipoles form, as shown by the gray symbols in the figure. The dipoles attract and *bind* some of the free charges on the plates. These newly bound charges are the ones that are circled in the figure. Thus, only a portion of the original free charges remain to contribute to the voltage across the plates. The relative permittivity ε_r is then defined as $Q' = Q/\varepsilon_r$ where $\pm Q'$ is the total *free charge* that remains after the dielectric material is added. Note that $Q' < Q$. The free charge density is similarly reduced to $s' = s/\varepsilon_r$. The total bound charge is $Q - Q' = Q(1 - 1/\varepsilon_r)$. Still no current flows across the plate since the added material is non-conductive. The capacitor continues to store electrical energy and the plates do not discharge.

Now suppose the space between the plates is filled by a dielectric material that also has a non-zero electrical conductivity σ. In this case, some of the free charges are able to migrate through the material between the plates, and hence an electric current is created in accordance with Ohm's law $\mathbf{J} = \sigma\mathbf{E}$. The capacitor, in this case, is *leaky* and loses some of its stored electrical energy. The electric field **E** is given, as usual, in terms of the free charge density by $E = s\hat{\mathbf{z}}/\varepsilon_0$. A new *displacement field* **D** is defined in terms of the *total* charge density as $D = s\hat{\mathbf{z}} = \varepsilon_0\varepsilon_r E = \varepsilon E$. The physical interpretation of the displacement field is explained as follows.

Suppose an external electric current of density **J** [A/m^2] charges the plates. The total surface charge density s increases with time as charges are brought up to the plate by the external current. The increase in charge density, in the case of a pure non-conducting dielectric, is given by $J = (ds/dt)\hat{\mathbf{z}} = (dD/dt)$. In the case $\sigma = 0$, all the charges are stopped on the plate and no current is conducted across. Nevertheless, there is a *displacement current* of magnitude $d\mathbf{D}/dt$. If the capacitor is filled with conducting material, some of the charges that are brought up to the plate by the external current **J** can migrate across to the other plate. Therefore, in this case there is also a *conduction current* given by Ohm's law. The total current is then the sum $\mathbf{J} = \sigma\mathbf{E} + d\mathbf{D}/dt$, where the magnitude of **D** is now scaled by the bound charge density $s - s'$. Sometimes the electric polarization vector $P = \varepsilon_0\chi_e E$ is introduced, in which χ_e is termed the *electric susceptibility*, and we write $D = \varepsilon_0 E + P$. However, we will find no further occasion to use the electric polarization vector **P**.

The displacement current, and its distinction from the conduction current, is usefully described by the simple parallel-plate model considered above. However, the geophysical situation may be better conceptualized with reference to Figure 9.7 in which an AC voltage $V\exp(i\omega t)$ is applied across a rock mass. The rock has electromagnetic properties (σ, ε_r) and thus both a conduction current $\sigma\mathbf{E}$ and a displacement current $d\mathbf{D}/dt$ will be present. There are both energy-storage and energy-loss mechanisms. It is well known in the history of physics (e.g. Selvan, 2009) that the presence of the energy-storage term, associated with the displacement current, led Maxwell to predict the existence of electromagnetic waves.

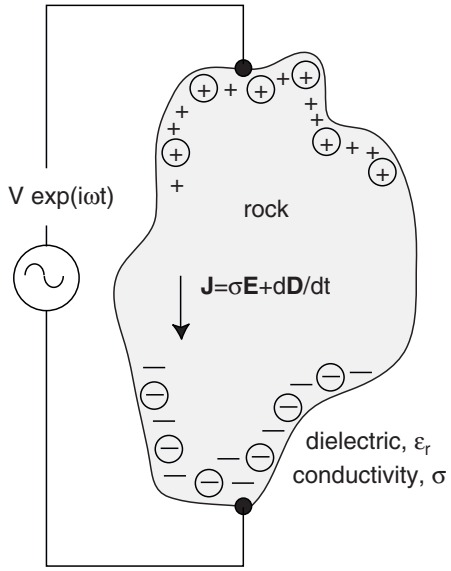

Figure 9.7 Conceptual model of a rock under an applied time-harmonic voltage.

If an AC voltage with harmonic-time variation exp ($i\omega t$) is applied to a rock mass, as shown, the total current in the frequency domain becomes $\mathbf{J} = \sigma\mathbf{E} + i\omega\mathbf{D} = \sigma\mathbf{E} + i\omega\varepsilon\mathbf{E} = \sigma^*\mathbf{E}$ where $\sigma^* = \sigma + i\omega\varepsilon$ is a *complex conductivity* that depends on frequency. Neglecting EM induction effects for the moment, the conduction current $\sigma\mathbf{E}$ is in phase with the driving voltage while the real component of the displacement current $i\omega\mathbf{D}$, generated by lossless polarzation effects, is out of phase. The dielectric loss term described in the previous section acts, however, mathematically, much like the Ohmic loss term and often in the literature it is seen that both are lumped together into the imaginary component of a complex permittivity $\varepsilon^*(\omega)$. However, it should be remembered that the two phenomena have distinct physical origins: Ohmic loss is essentially the kinetic energy loss of migrating quasi-free charges scattering off lattice ions, while dielectric loss is associated with the rotation of bound charges in a viscous fluid. As such, it is easy to see that the Ohmic term is sensitive largely to connected porosity while the dielectric loss term is more sensitive to total water content, which equals the total (connected and unconnected) porosity in a fully saturated system.

9.3 Dielectric properties of rocks and soils

The electrical properties of porous rocks, including the conductivity σ and the dielectric constant ε_r, are highly sensitive to the pore-scale microstructure and the volume fractions of the solid and fluid phases. The most important factor in determining the dielectric constant ε_r of near-surface geomaterials is the volumetric water content, θ_W. This is because water is characterized by $\varepsilon_r \sim 81$ and air by $\varepsilon_r = 1$ while the dielectric constant of the solid matrix material most commonly falls somewhere close to the range $\varepsilon_r \sim 3$–4. The empirical Topp equation (Topp *et al*., 1980)

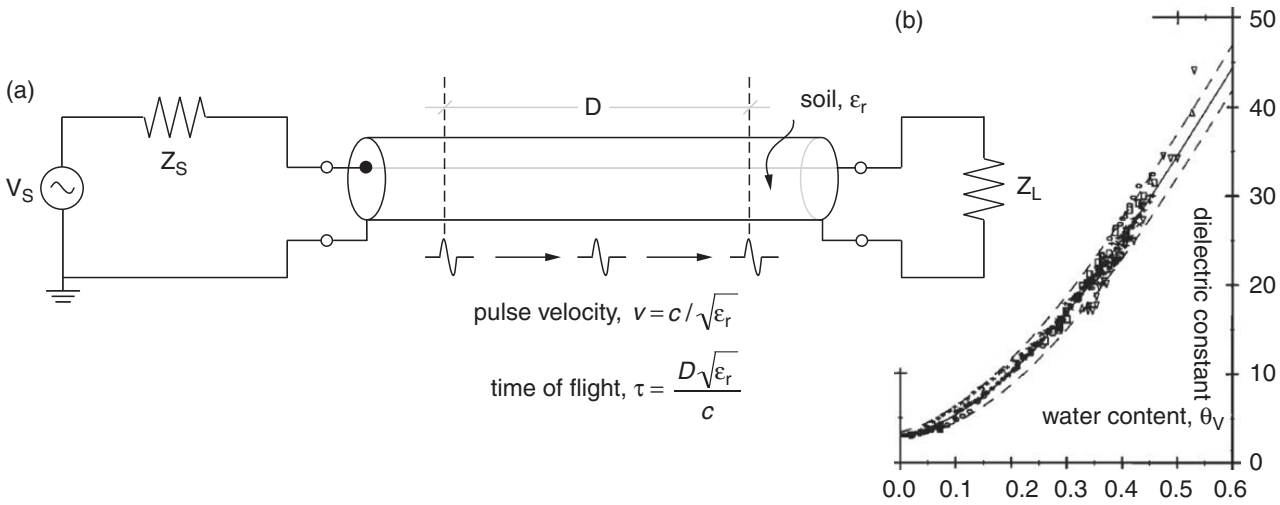

Figure 9.8 (a) Transmission-line method for determining soil dielectric constant; (b) soil dielectric constant as a function of moisture content for different soil types. After Topp *et al*. (1980).

$$\varepsilon_r = 3.03 + 9.3\theta_W + 146.0\theta_W^2 - 76.7\theta_W^3 \tag{9.4}$$

is a widely used formula for expressing the bulk dielectric constant of a soil as a function of its water content. It can be regarded as a GPR equivalent of Archie's law in the sense that it is based on a compendium of laboratory measurements using a wide variety of samples. The method for determining ε_r involves a time-of-flight measurement of an electromagnetic pulse propagating along a coaxial waveguide loaded with the soil sample, as shown in Figure 9.8a. The results from using soils of different types with varying water content θ_W are summarized in Figure 9.8b, in which the curve given by Equation (9.4) and an estimate of its experimental uncertainty are overlain. The Topp equation works well in clays and loams but has less predictive capabilities for organic-rich soils.

The effect of salt content on the bulk ε_r of water can become significant at high values of salinity. In general, ε_r drops with increasing salinity, to values as low as ~ 60 for highly saline pore waters of ~ 100 parts per thousand (ppk) (Hizem *et al*., 2008). There are three effects at work: (i) more salt by volume implies fewer polarizable water molecules; (ii) water molecules cannot rotate as easily if they are weakly bound to Na and Cl ions; (iii) mobile Na and Cl ions within the pore-fluid electrolyte agitate the water molecules, tending to randomize alignment of the H_2O dipole moments. Hizem *et al*. (2008) also note that ε_r of water drops with increasing temperature T to as low as ~ 45 (at 150 °C) due again to thermal agitation of the H_2O dipole moments.

Many heuristic dielectric mixing rules have appeared in the literature. The heuristic rules, by definition, do not have a firm theoretical basis. The complex refractive index model (CRIM), for example, is based simply on a volumetric averaging of the dielectric constants of the constituents of a composite material (Tsui and Matthews, 1997). The CRIM formula for the dielectric constant ε_r of a partially saturated rock is

$$\sqrt{\varepsilon_r} = \phi(1 - S_W)\sqrt{\varepsilon_0} + (1 - \phi)\sqrt{\varepsilon_1} + \phi S_W\sqrt{\varepsilon_2}, \tag{9.5}$$

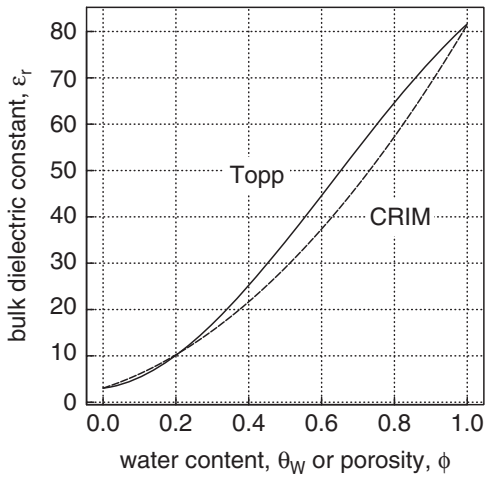

Figure 9.9 Bulk dielectric constant of saturated vesicular basalt as predicted by the Topp and CRIM equations.

where ϕ is the porosity, S_W is the water saturation, ε_1 is the dielectric constant of the matrix material, and ε_2 is the dielectric constant of the pore water. Often, however, CRIM provides unsatisfactory estimates of the bulk dielectric constant since it does not take into account the geometric arrangement of the various solid and fluid phases that make up the composite material (West *et al.*, 2003).

Consider a fully water-saturated vesicular basalt as an idealized system composed of fluid spheres of dielectric constant $\varepsilon_2 = 81.5$ embedded within a solid matrix of dielectric constant $\varepsilon_1 = 3.03$. The bulk dielectric constant ε_r of the composite system, as a function of the volumetric water content, is shown in Figure 9.9 using the Topp equation (9.4) and the CRIM equation (9.5).

A number of more rigorous, physics-based dielectric mixing rules have been developed using an effective medium approach. One of these is the Maxwell–Wagner–Bruggeman–Hanai (MWBH) model (Chelidze and Gueguen, 1999), which grew out of original work by Maxwell in the nineteenth century. The MWBH model treats the composite material as a spatially uniform, concentrated suspension of spherical particles of dielectric constant ε_2 embedded within a host medium of dielectric constant ε_1. The MWBH relationship between the effective dielectric constant ε_r of the composite medium and the dielectric constants of its constituents is

$$\frac{\varepsilon_r - \varepsilon_2}{\varepsilon_r - \varepsilon_1}\left(\frac{\varepsilon_1}{\varepsilon_r}\right)^{1/3} = 1 - \Phi_2, \tag{9.6}$$

where Φ_2 is the volume fraction of the spherical inclusions. Note that the dielectric constants ε_1 and ε_2 appearing in Equation (9.6) can actually be complex functions of frequency. Robinson and Friedman (2001) have developed a formula that predicts the bulk dielectric constant of mixtures containing n different grain sizes.

The mixing theories described above do not take into account surface electrical-polarization processes that might occur on the interfaces between two components of the mixture. These surface effects are likely to be important factors in determining the effective dielectric constant of actual porous near-surface geomaterials. For example, the Maxwell–Wagner effect

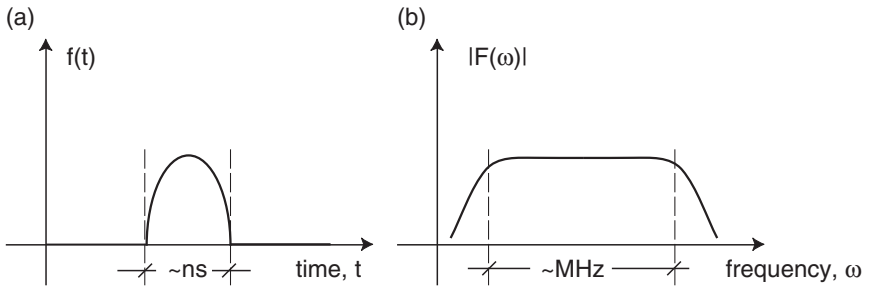

Figure 9.10 (a) Transmitted pulse in the time domain. (b) Broadband amplitude spectrum.

increases with increasing hydrocarbon saturation in a three-phase oil–water–sand mix due to the appearance of additional oil–water interfaces. A good discussion of surface effects on the dielectric properties of porous rocks can be found in Chelidze and Gueguen (1999).

9.4 Resolution

The *resolution* of a GPR system ultimately depends on its capacity to distinguish between two radar returns that are spaced closely in time. The two returns could be due, for example, to the top and bottom interfaces of a buried thin layer. Hence, the resolution is determined by the transmitted pulse width Δt, along with any broadening and distortion of the pulse as it propagates into the subsurface. As the pulsewidth of a given TX decreases, its frequency bandwidth Δf increases (Figure 9.10). The pulsewidth–bandwidth trade-off is a general principle of Fourier analysis, as has been well documented in the seismic literature (Knapp and Steeples, 1986). Therefore, a high-resolution GPR necessarily transmits a broad band of frequencies. Resolution is improved by transmitting at higher frequencies only if the bandwidth is simultaneously increased. This can be achieved in the time domain by narrowing the pulse width. A pulse radar operating in the megahertz range generally has a bandwidth of a similar magnitude and a pulse width of $\Delta t \sim$ 1–10 ns.

There is also a trade-off between range and resolution in GPR systems. As was shown earlier in Figure 9.5b, attenuation increases with frequency beyond about ~ 100 MHz. Sharpening the resolution by narrowing the pulse width invariably comes at the cost of a reduction in the depth of penetration at which the subsurface targets may be interrogated. The range–resolution trade-off places a fundamental limitation on the capability of GPR to image small-scale structures at depth.

9.5 Data acquisition

A standard geophysical surveying geometry for GPR is the common-offset configuration (Figure 9.11a) in which the transmitter and receiver antennas are moved in tandem along a profile while maintaining a fixed separation distance between them. The WARR

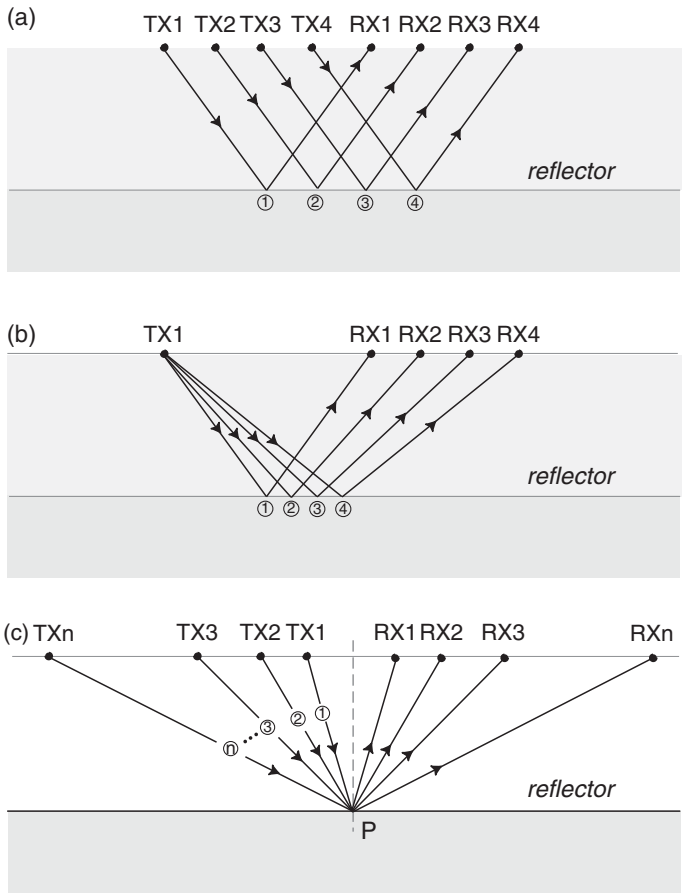

Figure 9.11 (a) Common-offset GPR profiling; (b) wide-angle radar reflection, WARR; (c) common depth-point configuation, CDP.

configuration (Figure 9.11b) is analogous to the deployment of a seismic geophone array except that typically only a single receiver is available and it is stepped out from the fixed transmitter location, as shown. The WARR configuration is not as popular as common-offset sounding since attenuation in the ground is often sufficiently high that good quality data from large TX–RX offsets cannot be acquired. The common depth-point (CDP) configuration is shown in Figure 9.11c. It is often used to estimate the ground radar velocity v by determining the normal moveout of radar return signals, as in the seismic-reflection technique. A new generation of GPR systems, presently under active development and beginning to appear in commercial offerings (e.g. the Sensors and Software product SPIDAR, see www.sensoft.ca/products/spidar/spidar.html), consists of multiple transmitter and multiple receiver antennas working simultaneously. Such systems increase the efficiency of data acquisition in the field, thereby enabling a lower cost and/or an increased scope of a project.

The antennas can be arranged in broadside, in-line or cross-polarized orientations, as shown in Figure 9.12. Due to the vectorial nature of electromagnetic waves, each of the orientations provides a different illumination of buried targets. A discussion on radar target polarization effects appears later in this chapter. A photograph showing in-line 100 MHz GPR data acquisition with 1.0 m TX–RX separation is shown in Figure 9.13.

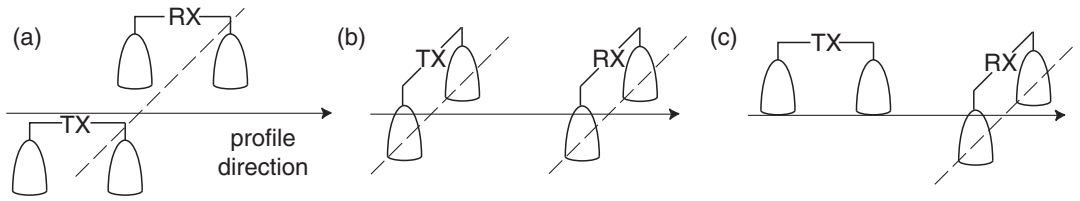

Figure 9.12 GPR antenna orientations: (a) broadside; (b) in-line; (c) cross-polarized relative to the data-acquisition-profile direction.

Figure 9.13 In-line 100 MHz GPR data acquisition with a 1.0-m TX–RX separation distance.

9.6 Basic GPR data processing

A number of standard data-processing steps should be performed after data acquisition in order to transform measured radargrams into a time or a depth section that is ready for advanced processing, qualitative interpretation, and attribute analysis. The standard processing steps described below are recommended in most cases but they do not all have to be performed or in the particular order given. It should be kept in mind that each data-processing step results in a loss or transformation of the information that is contained in the original radar data. Thus, processing should always be performed carefully and, in the final analysis, it becomes a subjective process.

Although it is tempting to apply standard seismic data-processing algorithms (Yilmaz, 2001) to GPR data, significant interpretation errors can be made since the nature of subsurface radar wave propagation is very different from that of seismic wave propagation. As pointed out by Cassidy (2009), GPR signals exhibit considerably more attenuation, dispersion, and scattering from heterogeneities than do seismic signals. The spatial variations in electromagnetic properties of geomaterials are moreover much stronger than variations in

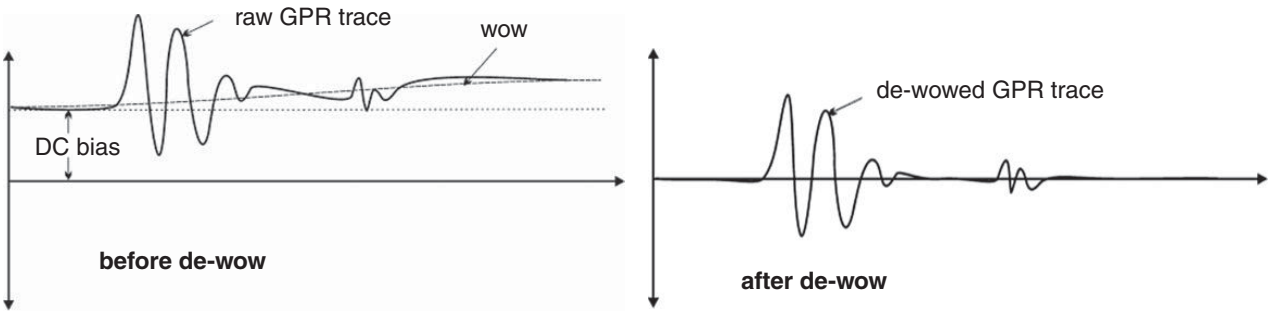

Figure 9.14 Effect of de-wow filter. After Cassidy (2009).

elastic properties; hence, GPR wavefronts generally exhibit more geometric complexity than is found in seismic wavefronts. The GPR waves are also vectorial so that changes in polarization as the wave propagates, reflects, refracts, diffracts, and scatters must be taken into account. Antenna design and ground coupling further contribute to complexities that are specific to GPR wave propagation and these have no exact seismic counterpart.

The first step of GPR data processing is file reconciliation and trace editing. The former is done to bring the datafiles that were actually recorded in the field into the desired survey format. For example, some of the profiles may have been acquired in the reverse direction or acquired out of the correct sequence. Some of the datafiles may be redundant, or there may be some files that are unusable due to equipment malfunctions, poor acquisition protocol, or excessive external noise. Bad traces within a profile may need to be removed. Some profiles may contain extra traces, or too few traces, due to navigation errors. The extra traces can be deleted. The missing traces can be restored by interpolating from neighboring traces. These steps are necessary as most processing algorithms require uniform station spacing. Filtering, as discussed in Chapter 2, may be used at this stage to remove noise spikes and some of the extraneous energy from noise sources whose dominant frequencies lie outside the GPR bandwidth.

An essential GPR processing step to be performed early in the processing sequence, after file reconciliation, trace editing, and preliminary filtering, is the *time-zero correction*. Here, the measured radar traces along a profile are individually shifted along the time axis such that a recognizable feature that is common to each trace, typically the first peak of the earliest arriving pulse train, is aligned to a common temporal datum. Trace misalignment is caused by many factors, including drift in the transmitter or receiver electronics, irregularities in either the cables connecting the transmitter and receiver electronics to the antennas, or in the connectors themselves; or else small, along-profile variations in TX–RX antenna spacing and orientation. The time-zero correction improves the spatial coherency, or cross-trace correlation, of the resulting time section and readies it for further processing.

A *de-wow* low-cut filter should also be applied as one of the early GPR data-processing steps. "Wow" is the ubiquitous slow variation of the baseline amplitude found in radar traces, and includes any bias, or constant shift, in the baseline amplitude (Figure 9.14, left). The baseline amplitude of a radar trace, at large values of the two-way traveltime, ideally should be a constant zero. Wow variation is caused by the presence of unwanted low-frequency components contained in the spectrum of the transmitted electric field, and also by EM induction effects in the conductive ground. The de-wow filter attenuates these

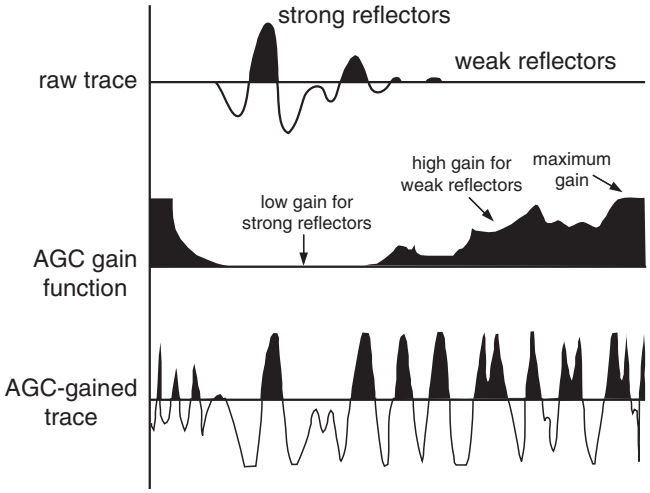

Figure 9.15 The effect of an AGC function applied to a radar trace. See www.sensoft.ca/products/spidar/spidar.html

Figure 9.16 500 MHz GPR data. The left panel shows raw traces, while the right panel shows the same data after background removal and gain control.

low-frequency components to produce a zero baseline amplitude. The effects of a de-wow filter are shown in Figure 9.14, right.

As in seismic data processing, *gain control* functions can be applied to radar traces in order to correct for geometric spreading and attenuation of the propagating wavefront, and to equalize the signal returns from all depths. There are many different types of gain functions that could be applied. An automatic gain control (AGC) function, for example, is a simple multiplier that scales with the inverse of the signal strength of the raw trace. The effect of applying an AGC function to a raw trace is shown in Figure 9.15. The objective of applying such an AGC function is to enable visualization of both shallower and deeper reflectors on radar sections at roughly the same display intensity.

A *background-removal filter* involves the subtraction, from each radar trace, of a lateral moving average of the radar amplitudes over a given early-time window. This filter mitigates the unwanted appearance of ground clutter or antenna ringing in displayed radar sections. Ground clutter is the high-amplitude, laterally continuous signal seen in radar sections at early time (Figure 9.16, left). Ground clutter is caused by direct coupling, or cross-talk, between the TX and RX antennas and contains no useful subsurface information. The background removal filter cleans up the early portion of the radar section and sometimes permits a better visualization of very shallow reflectors. A deleterious effect of

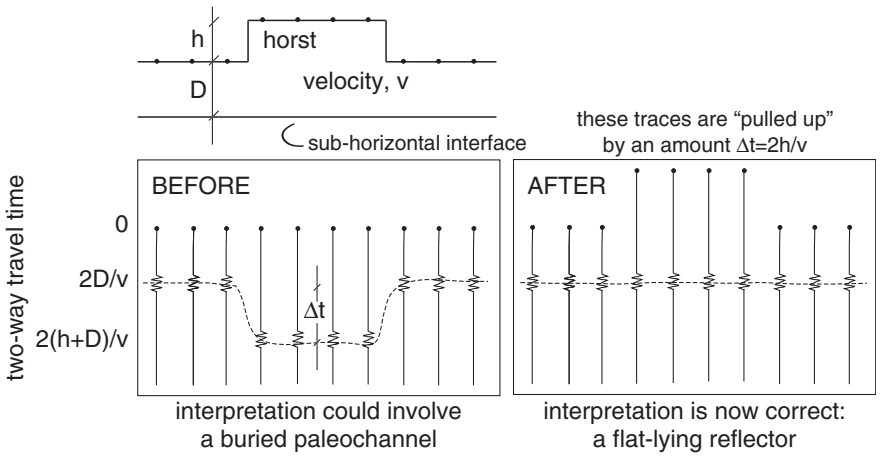

Figure 9.17 Schematic illustration of GPR topographic correction.

background filtering, however, is that it can also remove much of the signature of slowly undulating soil horizons and other near-surface geological features, which could include top of bedrock or the water table. Thus, background removal should be used with care or avoided if shallow soil stratigraphic, structural, or hydrostratigraphic mapping is an objective of the GPR survey.

A radar time section processed using a background removal filter and gain control is shown for illustrative purposes in Figure 9.16, right. The ground clutter is largely attenuated and the deeper reflectors are much better imaged in the processed time section.

Elevation measurements should be made along GPR profiles that traverse irregular terrain. A *topographic correction* can then be made to account for the distortion in the acquired radargram due to the along-profile elevation changes. A simplified illustration of a GPR topographic correction is shown in Figure 9.17. Suppose the geology consists of a subhorizontal interface buried at depth D beneath a horst of height h. The radar velocity of the upper unit is known or estimated to be v. An idealized, uncorrected radargram is shown at left. A naive geological interpretation that does not take elevation into account could involve a buried paleochannel, as shown by the dotted line. The topographically corrected radargram is shown at right. The elevation data, combined with the knowledge or estimate of the radar velocity v, are used to "pull up" the traces that were acquired over the horst structure by an amount $\Delta t = 2h/v$. The correct interpretation of a flat-lying radar reflector can now be made.

A field example from Cassidy (2009) is shown in Figure 9.18. The data were acquired over the lobe of a pyroclastic flow. Notice in the topographically corrected section, at right, that the main reflecting horizons (marked as *key basal surfaces*) appear more flat-lying, and are closer to their correct stratigraphic positions. The topographically corrected radargram thus allows a more reliable geological interpretation than does the uncorrected radargram.

A CDP analysis is performed by symmetrically expanding the TX and RX antennas about a common midpoint (Figure 9.11c, bottom). A flat-lying subsurface reflector would exhibit a normal hyperbolic moveout in the radar time section, analogous to the previously discussed seismic case (see Chapter 6). As in the seismic case, the subsurface velocity is the one that, when used in an NMO correction, best flattens out the reflector. Alternatively,

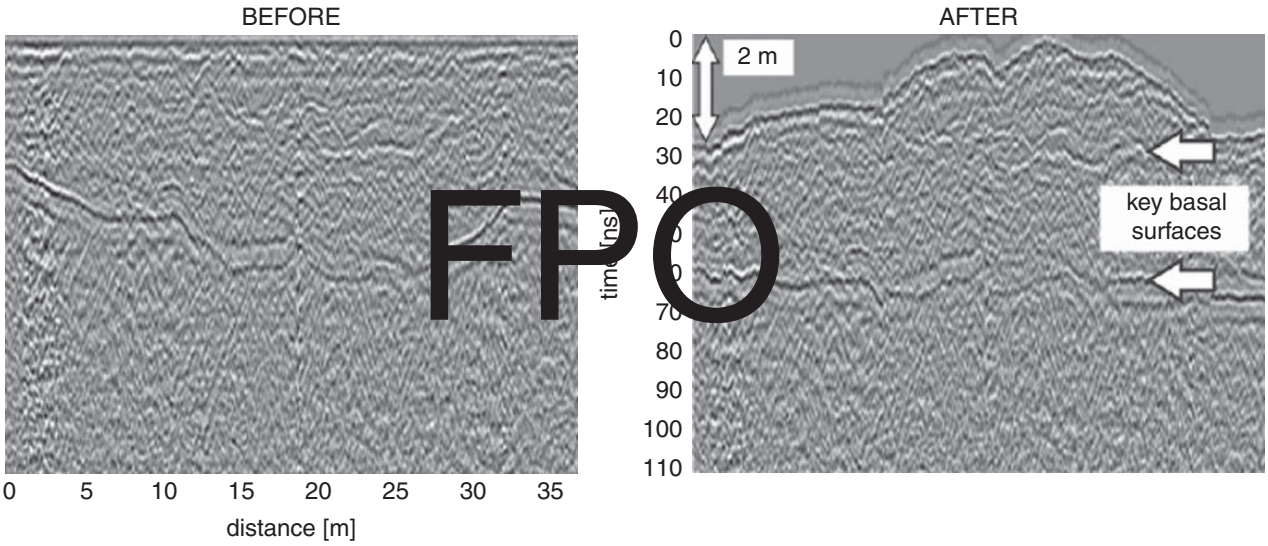

Figure 9.18 225 MHz GPR data. The left panel shows original radargram; right panel, after topographic correction. After Cassidy (2009).

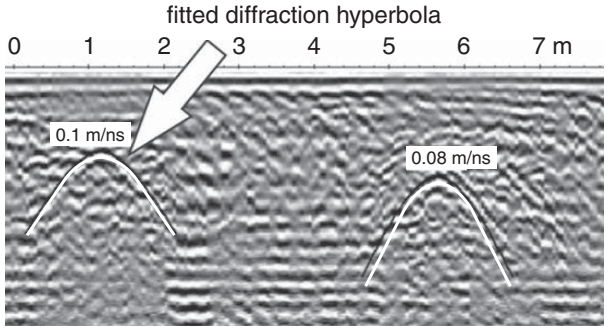

Figure 9.19 Radar velocity analysis by diffraction hyperbola fitting. After Cassidy (2009).

the subsurface velocity can be estimated by fitting a hyperbolic function to observed diffractions in a radar time section (see Figure 9.19). Once the subsurface radar velocity is known, by either of these methods, the practitioner is enabled to make a *time-to-depth conversion*. Then, one can display a radar depth section rather than a time section. The advantage of a depth section is that the radar reflection horizons presumably appear at their actual depth beneath the surface.

9.7 Advanced GPR data processing

Advanced processing steps are not always required but are briefly summarized here for the convenience of the reader. Most often, the basic processing steps outlined above are sufficient to make a useful geological interpretation. Advanced processing methods include deconvolution, *f–k* filtering, and migration.

Deconvolution is the process of removing the effect of the transmitted source wavelet from the measured radar traces, in an attempt to expose the idealized impulse response of subsurface layers. A discussion of convolution and deconvolution, mainly in the context of seismic data processing, appears in Chapters 2 and 11, respectively. Since the source wavelets of GPR are considerably more complex than their seismic counterparts, and the medium is dispersive, deconvolution is more challenging and therefore is used infrequently in GPR data processing.

The *f–k* filter operates as a bandpass filter in both time and space simultaneously. The two-dimensional (2-D) spatiotemporal radar data are first Fourier transformed into the frequency–wavenumber, or (f, k) domain. Then, a pass region in (f, k) is selected. Energy outside the pass region is attenuated and then the data are inverse-Fourier transformed back into the original time–space (t, x) domain. This filter can be used to suppress or enhance dipping events depending on their orientation.

A multitude of seismic migration algorithms have been developed with great success in petroleum exploration geophysics (e.g. Etgen *et al*., 2009). The main goal of migration is to undo the effects that the finite-velocity wave propagation bestows on measured time sections. Specifically, migration collapses diffractions back to their causative point sources and re-positions dipping events to their correct subsurface locations (see Chapter 6 for further details). Migration requires that the subsurface velocity is known; this is usually estimated in GPR by a common midpoint (CMP) analysis or the diffraction-fitting procedure described above. A seismic migration algorithm however cannot be bodily taken over and applied to GPR data owing to the vectorial nature of electromagnetic wave propagation. Instead, specifically designed *vector migration* algorithms must be developed. These are presently under active investigation (e.g. Streich and van der Kruk, 2007; Streich *et al*., 2007). Successful schemes must take into full account polarization effects and antenna radiation patterns.

9.8 Electromagnetic plane waves

A practical understanding of the GPR technique is enhanced by a basic knowledge of the underlying theory of electromagnetic wave propagation in conductive media. The classical equations that govern the behavior of electromagnetic (**E**, **B**) fields in source-free regions are the Maxwell equations

$$\nabla \times H = J + \varepsilon \frac{\partial E}{\partial t}; \tag{9.7}$$

$$\nabla \times E = -\frac{\partial B}{\partial t}; \tag{9.8}$$

where ε is the dielectric permittivity of the medium, along with the constitutive relations

$$J = \sigma E; \tag{9.9}$$

$$B = \mu H; \tag{9.10}$$

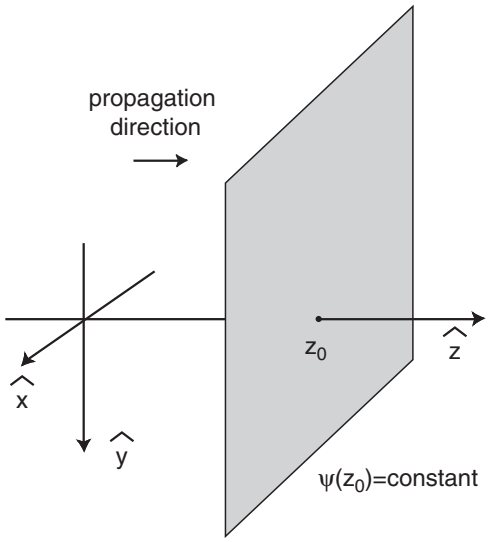

Figure 9.20 Snapshot of a planar wavefront, which moves to the right with velocity v.

where σ is the electrical conductivity and μ is the magnetic permeability of the medium. Following Wangsness (1986), we eliminate the magnetic field **B** from the above set of equations, giving rise to the *vector damped wave equation* for the electric field **E**,

$$\nabla^2 E - \mu\sigma \frac{\partial E}{\partial t} - \mu\varepsilon \frac{\partial^2 E}{\partial t^2} = 0; \tag{9.11}$$

while there is a similar damped wave equation for **B**.

Any Cartesian component $\psi = (E_x, E_y, E_z, B_x, B_y, B_z)$ of the electric **E** or magnetic **B** fields satisfies the *scalar damped wave equation*

$$\nabla^2 \psi - \mu\sigma \frac{\partial \psi}{\partial t} - \mu\varepsilon \frac{\partial^2 \psi}{\partial t^2} = 0. \tag{9.12}$$

It should be noted that in spherical or cylindrical coordinates, the various components of (**E**, **B**) do not satisfy scalar dampled wave equations, as in Equation (9.12), since the unit vectors in these coordinate systems depend on position.

In a non-conducting medium ($\sigma = 0$), such as air to an excellent approximation, the damped wave equation reduces to an ordinary lossless wave equation

$$\nabla^2 \psi - \mu\varepsilon \frac{\partial^2 \psi}{\partial t^2} = 0. \tag{9.13}$$

In the most general situation, the scalar function $\psi = \psi(\mathbf{r}, t)$ is an arbitrary function of position and time. In the specific case of a plane wave, which we can assume without loss of generality to be propagating in the $\hat{\mathbf{z}}$ direction, the function ψ reduces to a planar wavefront form $\psi = \psi(z, t)$ such that for any x, y the function ψ is a constant (see Figure 9.20). Inserting the planar wavefront form into Equation (9.13) reduces it to the one-dimensional lossless wave equation

$$\frac{\partial^2\psi}{\partial z^2} - \frac{1}{v^2}\frac{\partial^2\psi}{\partial t^2} = 0, \tag{9.14}$$

where $v = 1/\sqrt{\mu\varepsilon}$ is the wave velocity.

In vacuum, the electromagnetic wave velocity assumes the light value $c = 1/\sqrt{\mu_0\varepsilon_0}$. In geological media, the magnetic permeability normally obeys $\mu_r > 1$ and dielectric permittivity similarly obeys $\varepsilon_r > 1$, such that the electromagnetic wave velocity is reduced relative to the speed of light.

The wave equation (9.14) can be conveniently solved using the *separation of variables* technique in which a solution is posited in the form $\psi = Z(z)T(t)$ as a product of a function of z only and a function of t only. Inserting the separable form $Z(z)T(t)$ into the wave equation (9.14) and re-arranging gives

$$\frac{1}{Z}\frac{\partial^2 Z}{\partial z^2} = \frac{1}{v^2}\frac{\partial^2 T}{\partial t^2} = -k^2, \tag{9.15}$$

where k^2 is a constant independent of z and t. Thus, the scalar wave equation has separated into two ordinary differential equations

$$\frac{\partial^2 Z}{\partial z^2} + k^2 Z = 0; \tag{9.16}$$

$$\frac{\partial^2 T}{\partial t^2} + \omega^2 T = 0; \tag{9.17}$$

where $\omega = kv$ is the angular frequency. The constant k is termed the *wavenumber*. The general solutions of Equations (9.16) and (9.17) are of the form $Z(z) \sim \exp(\pm ikz)$ and $T(t) \sim \exp(\pm i\omega t)$. A plane electromagnetic wave propagating in the $\pm\hat{\mathbf{z}}$ direction therefore has the form

$$\psi(z,t) = \psi_0 \exp(ikz - i\omega t). \tag{9.18}$$

Since ψ corresponds to any Cartesian component of the electromagnetic field (**E**, **B**) we can write

$$E(z,t) = E_0 \exp(ikz - i\omega t)\,\hat{\mathbf{y}}; \tag{9.19}$$

$$B(z,t) = -B_0 \exp(ikz - i\omega t)\,\hat{\mathbf{x}}; \tag{9.20}$$

where **E** and **B** are not independent of each other but are linked by the Maxwell equations. Note that **E** and **B**, as given by Equations (9.19) and (9.20) are completely *in phase* with each other, that is, their amplitudes wax and wane in tandem when viewed as a function of position or as a function of time. A sketch of the electromagnetic field associated with a propagating lossless electromagnetic plane wave is shown in Figure 9.21a.

The behavior of an electromagnetic plane wave changes fundamentally in a conducting (or lossy) medium, $\sigma \neq 0$. In this case, the one-dimensional scalar damped wave equation becomes

$$\frac{\partial^2\psi}{\partial z^2} - \mu\sigma\frac{\partial\psi}{\partial t} - \mu\varepsilon\frac{\partial^2\psi}{\partial t^2} = 0. \tag{9.21}$$

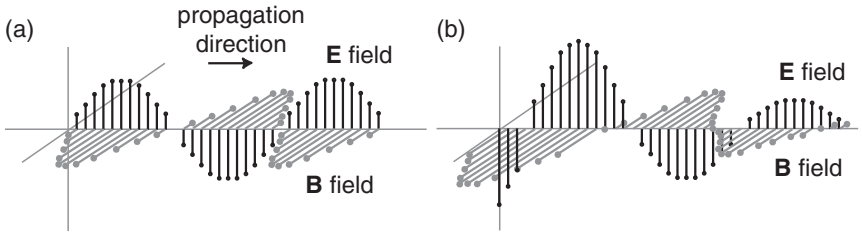

Figure 9.21 Electromagnetic plane-wave propagation: (a) lossless case; (b) lossy case.

Application of the separation of variables technique indicates that the separation constant k^2 generalizes to

$$k^2 = \omega^2\mu\varepsilon + i\omega\mu\sigma \tag{9.22}$$

such that the wavenumber is the complex quantity

$$k = \sqrt{\omega^2\mu\varepsilon + i\omega\mu\sigma} \tag{9.23}$$

which can be decomposed into its real and imaginary parts, $k = \alpha + i\beta$. These are readily shown to be, from Equation (9.23),

$$\alpha = \omega\sqrt{\frac{\mu\varepsilon}{2}}\left[\sqrt{1+\left(\frac{\sigma}{\omega\varepsilon}\right)^2}+1\right]^{1/2}; \tag{9.24}$$

$$\beta = \omega\sqrt{\frac{\mu\varepsilon}{2}}\left[\sqrt{1+\left(\frac{\sigma}{\omega\varepsilon}\right)^2}-1\right]^{1/2}. \tag{9.25}$$

Inserting the complex wavenumber $k = \alpha + i\beta$ into the scalar damped wave equation gives

$$\psi(z,t) = \psi_0\exp(-\beta z)\exp(i\alpha z - i\omega t); \tag{9.26}$$

which can be compared directly with the lossless case, Equation (9.18). An important aspect of electromagnetic plane-wave propagation in a conducting medium is the presence of the *attenuation factor* exp ($-\beta z$). In the diffusive regime $\sigma \gg \omega\varepsilon$, the parameter $\beta \to 1/\delta$ where δ is the electromagnetic skin depth introduced in the previous chapter. The oscillating function exp ($i\alpha z$) in Equation (9.26) is governed by the real part of a complex k, i.e. Equation (9.24), rather than the real constant $k = \omega\sqrt{\mu\varepsilon}$ as in the lossless case. The general form of the electric field **E** can be written as

$$E(z,t) = E_0\exp(-\beta z)\exp(i\alpha z - i\omega t). \tag{9.27}$$

In the lossless case, it follows directly from the Maxwell equations that the electric and magnetic fields are linked by the equation $B = (k/\omega)\hat{\mathbf{z}} \times E$. Thus, **E**, **B**, and $\hat{\mathbf{z}}$ form a mutually orthogonal triad. In the lossy case, the (**E**, **B**, $\hat{\mathbf{z}}$) vectors remain mutually orthogonal. However, since k is complex, the (**E**, **B**) vectors are no longer in phase with each other, as indicated by the sketch in Figure 9.21b. It is straightforward to demonstrate that the phase difference between **E** and **B** is Ω where

$$\tan\Omega = \sqrt{1+Q^2} - Q, \tag{9.28}$$

with $Q = \omega\varepsilon/\sigma$. The appearance of a phase difference between **E** and **B** is a consequence of the non-zero conductivity of the medium.

9.9 Plane-wave reflection from an interface

The electric or magnetic field at a point in space and time has both a magnitude and a direction and is thus a vector. However, the vectorial nature of electromagnetic waves is sometimes ignored by GPR practitioners. Polarization describes the orientation and magnitude of the field vector as the wave propagates and interacts with heterogeneities and buried targets. The polarization characteristics of GPR are useful for defining buried-target properties such as size, shape, orientation, and composition.

Suppose the **E**-field vector is always directed along a certain straight line. In that case, the **E** field is said to be linearly polarized. If the tip of the **E**-field vector instead sweeps out a circle as it propagates, it is circularly polarized. In the general case, the **E**-field vector is elliptically polarized. As described above, the electric **E** and magnetic **B** fields are mutually orthogonal to each other and to the direction of wave propagation. Let the direction of propagation be denoted again by $\hat{\mathbf{z}}$, in which case the electric field can be decomposed into two components

$$E_x(z,t) = E_{x0}\exp(-\beta z)\cos(\omega t - \alpha z - \varphi_X); \tag{9.29a}$$

$$E_y(z,t) = E_{y0}\exp(-\beta z)\cos(\omega t - \alpha z - \varphi_Y). \tag{9.29b}$$

The quantities E_{x0} and E_{y0} are the amplitudes of, respectively, the x and y components of the electric-field vector. Consider now a plane electromagnetic wave propagating in a general direction $\hat{\mathbf{p}}$ in a lossless, non-magnetic medium 1 characterized by dielectric constant ε_1. The wave is obliquely incident, with some incidence angle θ_i, onto a planar interface beneath which the medium 2 is characterized by a different dielectric constant ε_2, as shown in Figure 9.22. The problem is to determine the reflection and refraction coefficients.

The electromagnetic wave is said to be *horizontally polarized* if, as shown in Figure 9.22, the electric-field vector **E** points in the horizontal direction, i.e. the vector **E** lies in a plane that is perpendicular to the vertical plane of incidence. This is also known as the TE (transverse electric) mode of wave propagation. The magnetic-field vector **H** then lies in the vertical plane of incidence, as shown, and is orthogonal to the electric-field vector and the direction of propagation $\hat{\mathbf{p}}$. According to Figure 9.22, we have $\hat{\mathbf{p}} = \sin\theta_i\,\hat{\mathbf{x}} + \cos\theta_i\,\hat{\mathbf{z}}$.

The interaction of the incident plane wave with the interface is governed by the fundamental electromagnetic boundary conditions (continuity of the tangential components of the electric and magnetic fields) as well as Snell's law of refraction

$$\frac{\sin\theta_i}{\sin\theta_t} = \sqrt{\frac{\varepsilon_2}{\varepsilon_1}}, \tag{9.30}$$

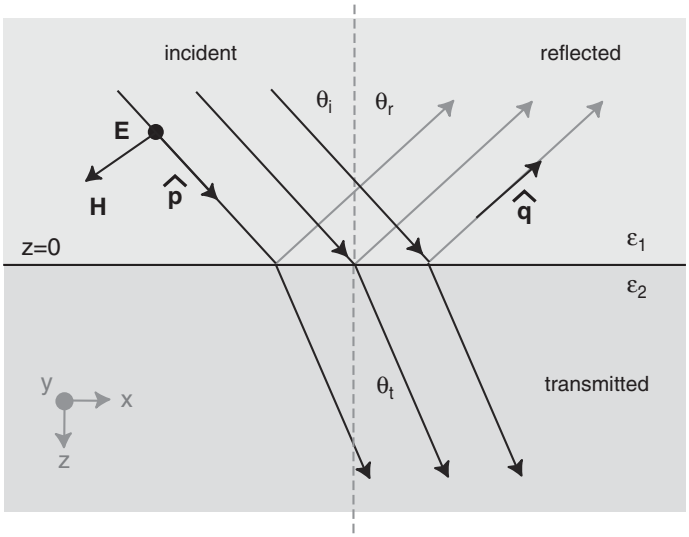

Figure 9.22 A horizontally polarized (TE-mode) plane electromagnetic wave obliquely incident upon a planar interface separating two lossless dielectric media.

and the law of reflection, $\theta_i = \theta_r$. The angle of transmission is θ_t and the angle of reflection is θ_r.

The lossless TE-mode electromagnetic plane wave propagating in the $\hat{\mathbf{p}}$ direction is described by an electric-field vector (of unit amplitude, for convenience)

$$E_i \tilde{} \exp(ik_1 \hat{\mathbf{p}} \cdot \hat{\mathbf{r}})\,\hat{\mathbf{y}} = \exp(ik_1[p_x x + p_z z])\,\hat{\mathbf{y}} = \exp(ik_1[x\sin\theta_i + z\cos\theta_i])\,\hat{\mathbf{y}}; \tag{9.31}$$

where we have made use in the last expression of the geometric identities $\cos\theta_i = p_z/|\mathbf{p}|$ and $\sin\theta_i = p_x/|\mathbf{p}|$, and $k_1 = \omega\sqrt{\mu_0\varepsilon_1}$ is the characteristic wavenumber of medium 1.

The total electric-field $\mathbf{E}^1$ in medium 1 is the sum of the incident field $\mathbf{E}_i$ and a reflected field $\mathbf{E}_r$ which propagates as a plane wave, according to the law of reflection, in the direction $\hat{\mathbf{q}} = \sin\theta_i\,\hat{\mathbf{x}} - \cos\theta_i\,\hat{\mathbf{z}}$. A reflection coefficient R is defined as the ratio of the amplitudes of the reflected and the incident electric fields, $R = |\mathbf{E}_r|/|\mathbf{E}_i|$. We have

$$E^1 = E_i + E_r = \exp(ik_1[x\sin\theta_i + z\cos\theta_i])\,\hat{\mathbf{y}} + R_{TE}\exp(ik_1[x\sin\theta_i - z\cos\theta_i])\,\hat{\mathbf{y}} \tag{9.32}$$

where the subscript TE on the reflection coefficient reflects the case of a horizontally polarized incident plane wave. Similarly, we can write the electric-field vector $\mathbf{E}^2$ in medium 2 as a transmitted wave

$$\mathbf{E}^2 = \mathbf{E}_t = T_{TE}\exp(ik_2[x\sin\theta_t + z\cos\theta_t])\,\hat{\mathbf{y}} \tag{9.33}$$

with transmission coefficient generally defined by $T = |\mathbf{E}_t|/|\mathbf{E}_i|$. It remains now to find the unknown TE-mode reflection and transmission coefficients (R_{TE}, T_{TE}) via application at the interface $z = 0$ of the fundamental electromagnetic boundary conditions.

Enforcing the continuity of the electric field, which is tangential to the interface since $\mathbf{E}$ is oriented in the $\hat{\mathbf{y}}$ direction, gives

$$\mathbf{E}^1|_{z=0} = \mathbf{E}^2|_{z=0}; \tag{9.34a}$$

$$\exp(ik_1 x\sin\theta_i) + R_{TE}\exp(ik_1 x\sin\theta_i) = T_{TE}\exp(ik_2 x\sin\theta_t).$$

The latter equation must hold for all x along the interface, including $x = 0$. In that case,

$$1 + R_{TE} = T_{TE}, \tag{9.35}$$

which provides the first constraint on the reflection and transmission coefficients. We now enforce continuity of the tangential magnetic-field component, H_x. An expression for H_x in terms of the electric field is obtained from Equations (9.8) and (9.10), keeping in mind the symmetry $E = E_y(x,z)\,\hat{\mathbf{y}}$,

$$\frac{\partial E_y}{\partial z} = i\mu\omega H_x. \tag{9.36}$$

Thus, continuity of H_x at the interface $z = 0$ is equivalent to

$$\frac{\partial \mathbf{E}^1}{\partial z}\Big|_{z=0} = \frac{\partial \mathbf{E}^2}{\partial z}\Big|_{z=0}. \tag{9.37}$$

Inserting Equation (9.37) into Equations (9.32) and (9.33) yields the second constraint on the unknown set of coefficients R_{TE} and T_{TE},

$$k_1 \cos\theta_i (1 - R_{TE}) = k_2 \cos\theta_t T_{TE}. \tag{9.38}$$

Solving Equations (9.35) and (9.38) for the reflection coefficient R_{TE} yields the final result

$$R_{TE} = \frac{\sqrt{\varepsilon_1}\cos\theta_i - \sqrt{\varepsilon_2 - \varepsilon_1 \sin^2\theta_i}}{\sqrt{\varepsilon_1}\cos\theta_i + \sqrt{\varepsilon_2 - \varepsilon_1 \sin^2\theta_i}}. \tag{9.39}$$

For the special case of normal incidence, $\theta_i = 0$, this expression reduces to a familiar form

$$R_{TE} = \frac{\sqrt{\varepsilon_1} - \sqrt{\varepsilon_2}}{\sqrt{\varepsilon_1} + \sqrt{\varepsilon_2}}, \tag{9.40}$$

which is the result earlier quoted in Equation (9.3).

The case of *vertically polarized*, or TM- (transverse magnetic-) mode wave propagation is characterized by an electric-field vector **E** lying in a plane that is parallel to the vertical plane of incidence. The TM-mode reflection coefficient is, by a similar analysis,

$$R_{TM} = \frac{\kappa\cos\theta_i - \sqrt{\kappa - \sin^2\theta_i}}{\kappa\cos\theta_i + \sqrt{\kappa - \sin^2\theta_i}}, \tag{9.41}$$

where $\kappa = \varepsilon_2/\varepsilon_1$. A graph of the reflection-coefficient amplitudes $|R_{TE}|$ and $|R_{TM}|$ as function of the incident angle θ_i, is given in Figure 9.23, for different values of the underlying dielectric ε_2. Equations (9.39) and (9.41) are known as the Fresnel equations.

Note that both amplitudes $|R_{TE}|$ and $|R_{TM}|$ approach 1.0, corresponding to total reflection, for grazing incident angles of $\theta_i \to 90^\circ$. Also, as expected, the reflection coefficients tend to vanish as the interface contrast $\kappa \to 1$, that is, $\varepsilon_2 \to \varepsilon_1 = \varepsilon_0$. Finally, for the TM mode, it is interesting to note that there exists a range of incident angles $\theta_i \sim 55$–70° over which there is no reflection.

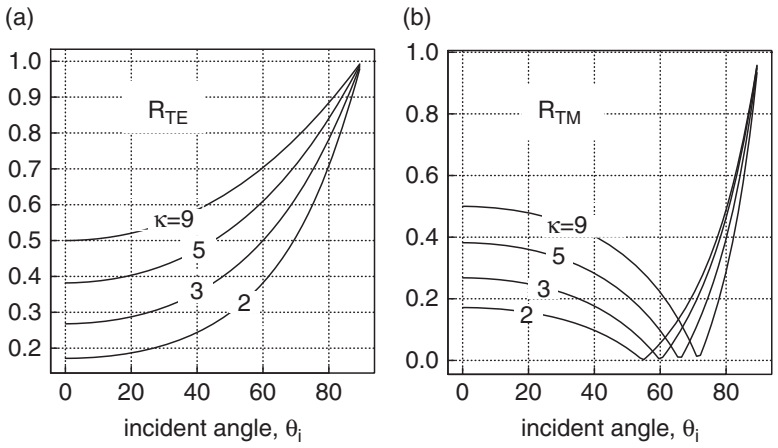

Figure 9.23 Reflection-coefficient amplitude for (a) TE-mode and (b) TM-mode plane waves as a function of incidence angle, with $\varepsilon_1 = \varepsilon_0$.

9.10 Analysis of thin beds

The detection of thin layers has long been of interest to explorationists engaged in seismic imaging of stratified petroleum reservoirs. Near-surface applications such as landslide hazard assessment or fractured-rock aquifer characterization also require imaging of thin subsurface rock layers as these sometimes define planes of slope instability or pathways for subsurface contaminant transport. The classic theoretical work on thin-bed analysis in seismology was performed by Widess (1973) who concluded that a bed as thin as $\lambda/8$ can be resolved, where λ is the dominant wavelength of the probing seismic signal. A more practical limit is suggested however by *Rayleigh's criterion* of $\lambda/4$. Below this limit, reflected signals from the interfaces at the top and bottom of the bed merge together and cannot be separated. Zeng (2009) recently showed that the practical resolution limit is affected by the shape of the source wavelet. Better resolution can be achieved with an asymmetric wavelet compared to a symmetric one.

Resolving a thin layer in GPR is more challenging than its seismic counterpart. The practical resolution limit is only ~ $3\lambda/4$ (Bradford and Deeds, 2006). The reduced capability of GPR to resolve thin layers owes mainly to the highly dispersive nature of the geological medium in which electromagnetic waves propagate. In a dispersive medium, a propagating wavelet rapidly becomes distorted and experiences large phase shifts upon reflection and transmission at material interfaces (Hollender and Tillard, 1998). Thus, it becomes difficult to recognize distinct returns from the top and bottom of a thin bed that have the same or similar shape as the transmitted wavelet. Detailed modeling of electromagnetic wave propagation in dispersive, heterogeneous geomaterials is normally required to determine whether a bed of a given thickness and material type can be resolved.

An important problem in GPR thin-bed analysis is to determine the bed reflectivity, since that can provide important information about the composition of the fill material. For example, the thin bed could be a fracture that contains a hazardous liquid contaminant. Consider the electromagnetic wave incident on a bed of thickness d and permittivity ε_2,

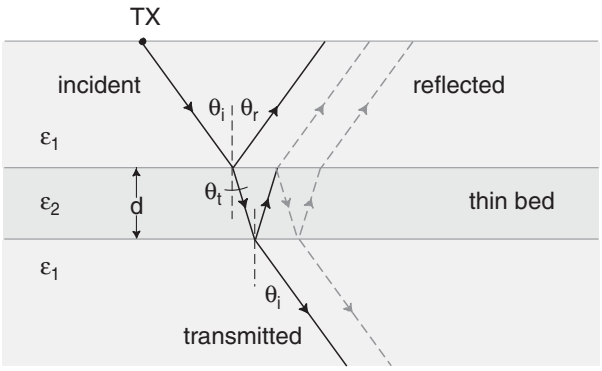

Figure 9.24 GPR reflection and transmission associated with a thin bed.

shown in Figure 9.24. The angles of incidence θ_i, reflection θ_r, and transmission θ_t obey Snell's law, Equation (9.30). The background medium has permittivity ε_1. The reflection and transmission coefficients depend on the polarization of the incident wave, as described in the previous section. Deparis and Garambois (2009) derive the following formula for the reflectivity of the thin layer,

$$R(\omega) = R_{12}(\omega)\,\frac{1 - \exp[-i\varphi(\omega)]}{1 - R_{12}^2(\omega)\exp[-i\varphi(\omega)]}, \tag{9.42}$$

in which $\varphi(\omega) = 2dk_2(\omega)\cos\,\theta_i$, and $R_{12}(\omega)$ is either the TE- or TM-mode reflection coefficient (Equation (9.39) or (9.41)), depending on the polarization of the incident wave.

It is easy to see that $R(\omega)$ given in Equation (9.42) reduces to its appropriate values for the limiting cases of a bed of zero thickness, and a bed of infinite thickness. Indeed, as $d \to 0$ it follows that $R \to 0$, which is the value that would be expected if the bed were absent. Also, as $d \to \infty$ one obtains $R \to R_{12}$, which is the correct form for a lower halfspace of dielectric permittivity ε_2.

While the theoretical expression for thin-bed reflectivity (Equation (9.42)) is quite simple, a number of idealizations were used in its derivation. Practically speaking, it is a difficult task to estimate reflectivity from measured amplitudes of GPR reflections (Bradford and Deeds, 2006; Deparis and Garambois, 2009). Factors that were not taken into account in the development of Equation (9.42) include: the shape of the source wavelet; the TX and RX radiation patterns; the coupling of the antennas to the ground; and scattering and reflection losses along the wave-propagation path. Despite these difficulties, Bradford and Deeds (2006) successfully analyzed GPR reflectivity variations with TX–RX offset, using a methodology similar to seismic amplitude versus offset (AVO) analysis (Castagna, 1993).

9.11 GPR antennas

Proper interpretation of GPR images can be modestly enhanced with a rudimentary understanding of the theory of antennas. An *antenna*, for our purposes, is a radiating current element whose dimensions are comparable to an electromagnetic wavelength. The

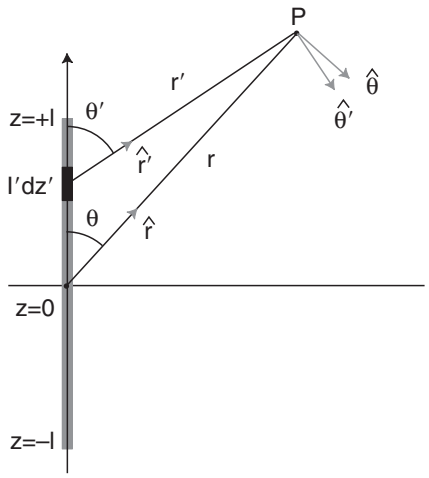

Figure 9.25 Calculation of the electric field of a long-straight-wire antenna carrying an oscillating electric current. After Wangsness (1986)

electric-current distribution, which is established by connecting the antenna to a power supply, is not uniform over the length of an antenna. Following Wangsness (1986), we consider the electromagnetic field radiated by a simple antenna consisting of a straight wire of length $2l$ oriented in free space in the $\hat{\mathbf{z}}$-direction. It is of interest to determine the electric field $\mathbf{E}(r, \theta)$ at some point in the far field, or *radiation zone*, defined by $kr >> 1$, where $k = \omega\sqrt{\mu_0\varepsilon_0} = \omega/c$ is the characteristic wavenumber of free space.

An oscillating electric dipole is equivalent to a current element so it is natural to visualize the long, straight antenna as an assemblage of current elements $I'(z')dz'$. We use an unprimed coordinate system to describe the position of an observation point P and a primed coordinate system to describe the position of a source point z', such as the one occupied by the current element $I'\mathrm{d}z'$ indicated in Figure 9.25. Each such current element $I'(z')dz'$ generates an electric field $d\mathbf{E}$, with the total electric field $\mathbf{E}$ being the superposition of the contributions from each of the constituent current elements.

The electric field $d\mathbf{E}$ of an oscillating infinitesimal dipole is well known and is of the form

$$d\mathbf{E} = -\frac{i\omega\mu_0 I'(z')dz'}{4\pi r'}\sin\theta'\exp(ikr' - i\omega t)\hat{\boldsymbol{\theta}}' \tag{9.43}$$

where

$$r' = \sqrt{r^2 + z'2 - 2rz'\cos\theta}, \tag{9.44}$$

and $\hat{\boldsymbol{\theta}}'$ is the unit vector perpendicular to $\hat{\mathbf{r}}'$. The total electric field $\mathbf{E}$ of the long straight antenna is readily obtained by integrating Equation (9.43) over the length of the antenna.

In the radiation zone we have $r >> \lambda$, where $\lambda = 2\pi/k = 2\pi c/\omega$ is the electromagnetic wavelength in free space. Let us also assume that we are interested in computing $\mathbf{E}$ at a distant point P such that $r >> 2l$. In that case, for any element z' of the antenna, the relationship $|z'| \ll r$ holds. In that case, Equation (9.44) reduces to

$$r' \approx \sqrt{r^2 - 2rz'\cos\theta} \approx r - z'\cos\theta, \tag{9.45}$$

where use has been made of the binomial approximation $\sqrt{1+x}\tilde{}(1+x/2)$ for $x << 1$. We can also use the approximation that $1/r\tilde{}1/r'$ for distant P, although we cannot likewise assume that $\exp(ikr')$ ~ $\exp(ikr)$. We also use the approximation for distant P that the polar unit vectors are parallel, $\hat{\boldsymbol{\theta}}' = \hat{\boldsymbol{\theta}}$. Putting all this together results in

$$\mathbf{E} = -\frac{i\omega\mu_0}{4\pi r}\sin\theta\exp(ikr - i\omega t)\hat{\boldsymbol{\theta}}\int_{-l}^{+l}\exp(-ikz'\cos\theta)I'(z')dz'. \tag{9.46}$$

This is the general expression for the electric field $\mathbf{E}$ in the radiation zone for a straight antenna of length $2l$ carrying an arbitrary electric current distribution $I'(z')$. The simplest GPR antenna is a *half-wave* antenna in which the length of the antenna is equal to one-half of the electromagnetic wavelength, that is, $l = \lambda/4$. The simplest electric current distribution for a half-wave antenna is the fundamental mode

$$I'(z') = I_0\cos kz', \tag{9.47}$$

in which the current vanishes at the ends of the antenna and is maximum at the center, $z' = 0$, where it is equal to$I'(z') = |I_0|$. The electric-current distribution given by Equation (9.47) vanishes at the ends of a half-wave antenna.

The electric field $\mathbf{E}$ for a half-wave antenna is now readily found by inserting the electric-current distribution, Equation (9.47), into the general expression, Equation (9.46). It is straightforward to integrate Equation (9.46) and hence to show that the electric field $\mathbf{E}$ radiated by a half-wave antenna, in the radiation zone, is given by

$$E = -\frac{ic\mu_0 I_0}{2\pi r\sin\theta}\cos\left(\frac{\pi}{2}\cos\theta\right)\exp(ikr - i\omega t)\hat{\theta}, \tag{9.48}$$

and that the electric field vanishes at all points P that are aligned with the antenna, i.e. at $\theta = 0$ and $\theta = \pi$. The radiation-zone electric field $\mathbf{E}$ pattern in free space looks very similar to the electric field of an infinitesimal dipole.

The electric-field distribution produced by a straight-wire antenna is affected substantially by the presence of the dielectric Earth. Consider an infinitesimal electric-dipole antenna lying on an air–soil interface in which the underlying medium is characterized by a permittivity $\varepsilon_1 = 4\varepsilon_0$ and conductivity $\sigma_1 \sim 0$, which is appropriate for a dry sandy soil. Suppose the horizontal electric dipole (HED) source is located in the plane of the page and directed to the right, as shown in Figure 9.26, left. The radiated electromagnetic field from this source has been computed using the finite-difference time-domain (FDTD) simulation code of Sassen (2009). The computations reveal that spherical waves propagate radially outward from the source into both the air and the soil. The electromagnetic wave velocities $v = 1/\sqrt{\mu\varepsilon}$ of the two media are different, hence the appearance of boundary waves to ensure continuity of tangential electric and magnetic fields across the interface. The boundary waves include a *head wave* propagating in the soil and an *evanescent wave* traveling in the air. The evanescent wave travels at the velocity of a ground wave and its amplitude decays exponentially with height above the interface. The head wave is the electromagnetic equivalent of a seismic critically refracted wave.

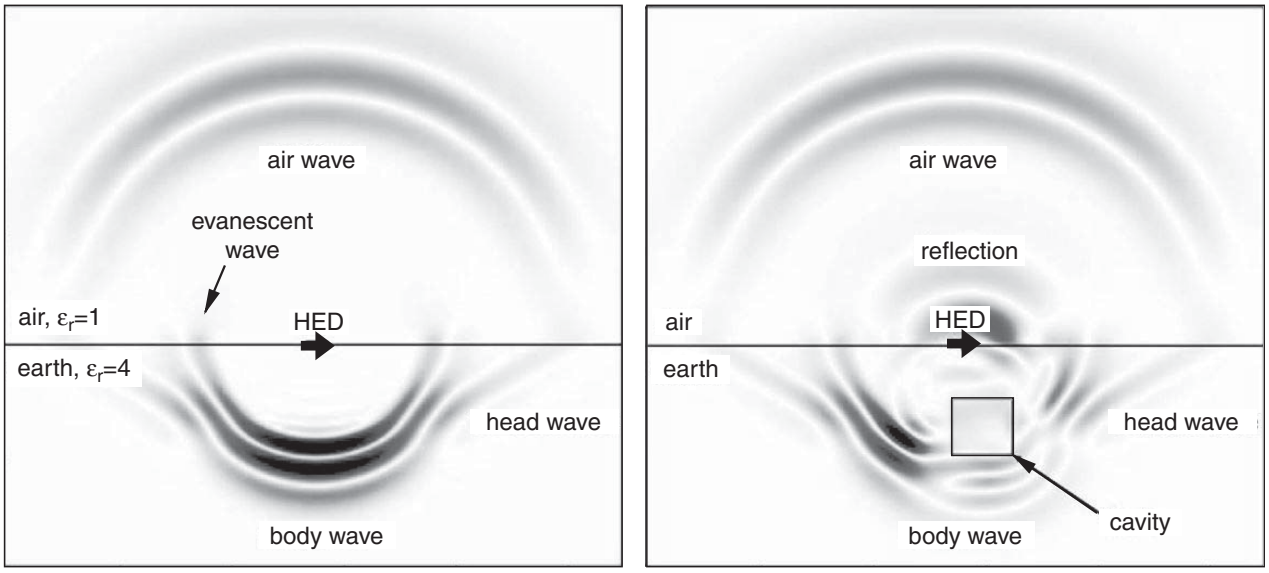

Figure 9.26 (Left) Snapshot of electric fields at $t = 9$ ns into a dielectric halfspace, shown in the vertical plane of the horizontal electric dipole (HED) source (300-MHz Ricker wavelet). (Right) Reflected and diffracted waves due to a 0.3-m^3 buried cavity. Plot dimensions: 2 m $\times$ 2 m. After Sassen (2009).

In Figure 9.26, right, the double-halfspace model is supplemented by a small air-filled cavity located in the ground. In this simulation, a reflected wave appears to be propagating back towards the GPR antenna and then upward into the air. The interaction of the primary double-halfspace field with the cavity also generates a complex pattern of refracted and diffracted body waves in the lower medium, as shown.

9.12 GPR radiation patterns

The previous section has demonstrated numerical solutions for GPR wave propagation in a heterogeneous lossless dielectric medium using the FDTD method. An analytic solution exists for the electromagnetic field radiated by a horizontal electric dipole lying on the interface between two semi-uniform dielectric media characterized by ε_0 (above) and ε_1 (below); it is given in the classic paper by Engheta *et al*. (1982).

The TE- and TM-mode radiation patterns of such a transmitter located on the surface of a ground with dielectric constant $\varepsilon_1 = 3.2\varepsilon_0$ are shown in Figure 9.27, top panel. The TE-mode pattern is the one that is generated when the dipole antenna is directed out of the page. The TM-mode pattern is generated when the dipole antenna lies within the plane of the page. The radiation patterns show, on an imagined vertical plane placed in the far-field in front of the page, how the electric-field strength changes as a function of direction relative to the antenna. The far-field is defined as any distance from the antenna for which $r \gg \max(l, \lambda)$, where l is the length of the dipole and λ is the radar wavelength. The radial axis on the polar plot is a logarithmic measure of relative field strength, relative to the field

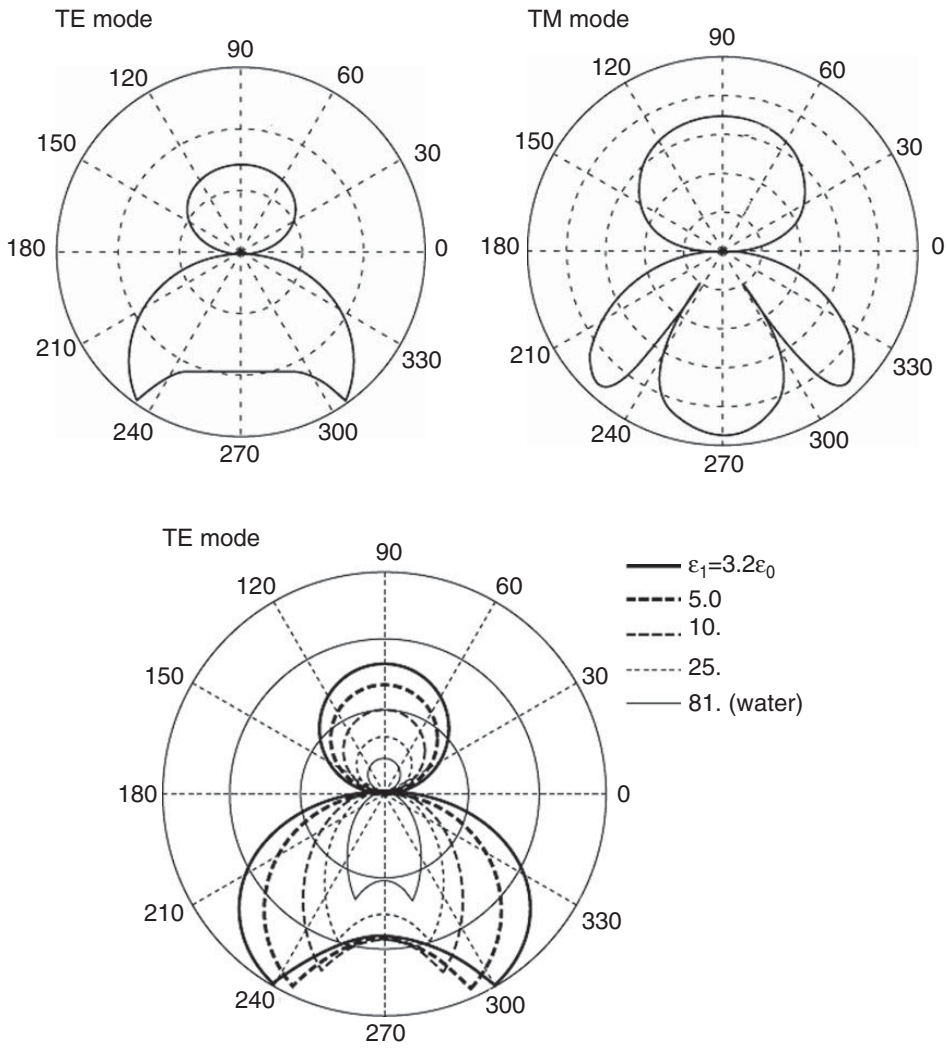

Figure 9.27 (a) Far-field TE- (top left) and TM- (top right) mode antenna directivity; (bottom) TE-mode antenna directivity as a function of ground permittivity. After Annan (2009).

strength at some reference point. For the present discussion, it suffices to note that the higher the field strength in a given direction, the further the radiation pattern extends toward the outer radius of the polar plot in that direction.

Both patterns show that electromagnetic energy is directed preferentially into the ground. Some of the energy, however, is directed uselessly into the air, adding unwanted noise to the GPR measurements. The leakage of signal into the air in some cases can be partially overcome (Annan, 2009) by carefully designing a proper shield to cover the antenna. The TE pattern shows that the greatest depth of signal penetration occurs at azimuths ~ 235° and ~ 305°. The TM pattern exhibits three subsurface lobes, along with two subsurface nulls located at ~ 240° and ~ 300°. The illumination of a buried target by the antenna is efficient if the target is located inside a lobe but inefficient if it is located inside a null region.

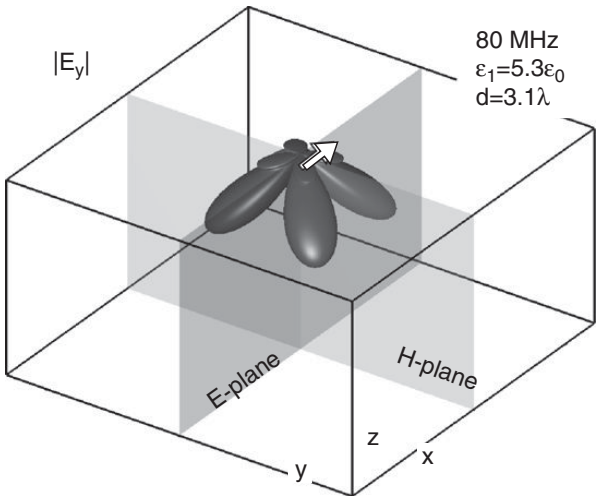

Figure 9.28 Example of a 3-D GPR radiation pattern. After Streich (2007).

The TE-mode radiation patterns that develop as the dielectric constant of the ground is varied between $\varepsilon_1 = 3.2\varepsilon_0 - 81\varepsilon_0$ is shown in Figure 9.27, bottom. It can be seen that electromagnetic energy spreads out laterally and vertically from the antenna as the ground dielectric constant decreases. This implies that the antenna scans a wider subsurface area in front of it when the ground dielectric constant is low. In other words, the antenna generally has a larger footprint in dry ground versus wet ground.

A visualization of the three-dimensional radiation pattern from an infinitesimal electric dipole located on a homogeneous dielectric, non-conducting subsurface is shown in Figure 9.28. A semi-analytic technique developed by van der Kruk (2001) was used for the calculation. The dipole in this case is oriented in the $\hat{\mathbf{x}}$ direction while the quantity plotted is the strength of the $\hat{\mathbf{y}}$ component of the electric-field vector **E** at a fixed distance 5.0 m (3.1 wavelengths) from the antenna, i.e. in the far-field. The projection of the 3-D pattern onto the "E-plane" would correspond to a TM-mode radiation pattern like the one shown in the previous figure, while a similar projection onto the "H-plane" corresponds to a TE-mode radiation pattern.

9.13 Target polarization

It is of interest to explore the interaction of a transmitted electromagnetic field with a compact subsurface target. The response of a cylinder is discussed here since elongated objects such as buried pipelines are commonly found in environmental and engineering geophysical surveys. Pipes scatter energy into preferential directions depending on the incident radar wave polarization relative to the orientation of the pipe. It is required that enough energy scatters from the target to reach the surface and permit a measurement by the receiver antenna (Radzevicius and Daniels, 2000). Preferential scattering may result in *depolarization* of the incident **E**-field, in which the scattered field has a different direction of polarization than the incident field.

To describe electromagnetic scattering from cylinders, it is intructive to consider the following two situations. The first is a TM-mode excitation in which the incident **E**-field

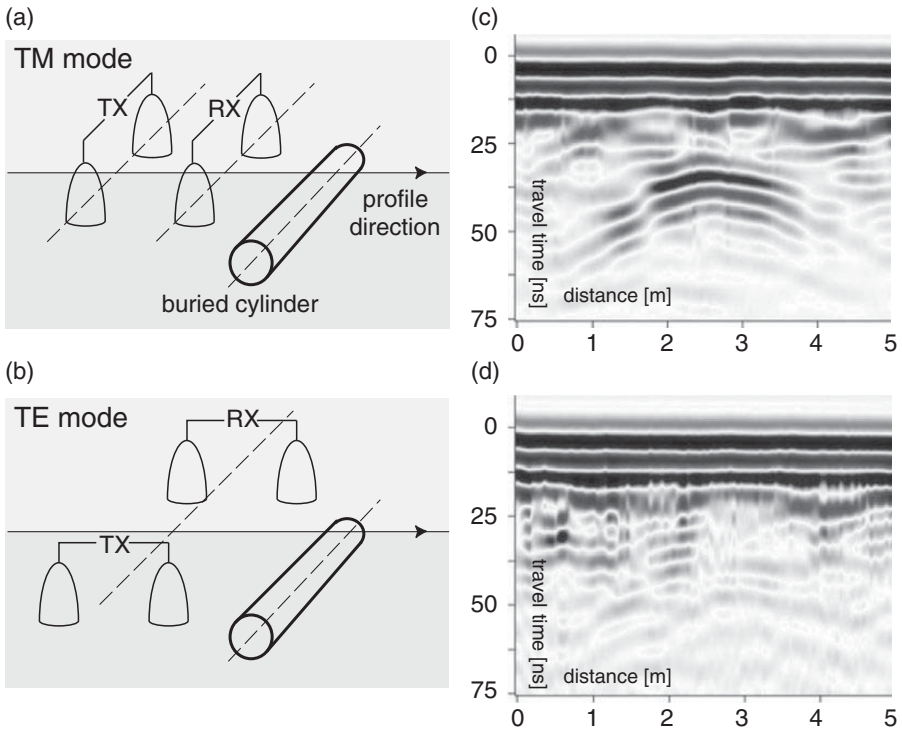

Figure 9.29 GPR survey configurations: (a) TM mode; (b) TE mode. GPR field data (200 MHz) of a pipe buried at 1.5-m depth in a silty sand soil showing the effect of TX and RX orientation relative to target, (c) TM mode; (d) TE mode. After Sassen and Everett (2005).

aligned with the long axis of the cylinder. The second is a TE-mode excitation in which the incident **E**-field is perpendicular to the long axis of the cylinder. As shown in Figure 9.29a, a TM-mode GPR survey is attained in practice when TX and RX dipole antennas are both aligned parallel to the long axis of the cylinder. A TE-mode survey configuration (Figure 9.29b) is attained when both are orthogonal to the long axis. In each case, the survey direction is orthogonal to the long axis.

To detect the pipe at the receiver antenna, the incident field must couple strongly with the cylinder and cause it to act as an efficient secondary radiator. The resulting scattered field must then contain a significant component that is in alignment with the RX dipole axis, since a RX dipole preferentially responds to that component. Consider first the TM-mode survey configuration. The field that radiates from the TX dipole is polarized mainly in the direction of the dipole axis. The incident field then propagates into the subsurface, with its polarization direction parallel to the long axis of the cylinder. There should follow a strong coupling with the target, since the incident electric field is mainly tangential to the long axis and this component is required by fundamental boundary conditions to be continuous across material interfaces. Since the incident field and the long axis of the target are aligned, there is almost no depolarization. Hence, the cylinder radiates a substantial scattered electric field that is polarized mainly in the same direction as the incident field. Accordingly, as shown in Figure 9.29c, a strong GPR signal is recorded by the RX dipole.

Now consider the TE-mode survey configuration. Here, the TX dipole axis is oriented in a direction orthogonal to the long axis of the cylinder. The incident field, since it is polarized in alignment with the TX dipole axis, should not couple strongly to the target since the tangential component of the field is very small. The cylinder in this case does not act as an efficient secondary radiator. Nevertheless, since induced currents flow most readily along the long axis of the cylinder, any scattered field that does emerge from the cylinder is likely to be polarized mainly along-axis. However, the RX dipole is oriented such that it most efficiently responds to scattered fields that are polarized across-axis. Accordingly, as shown in Figure 9.29d, the cylinder is not detected by the TE-mode experiment.

The foregoing conclusion applies to the GPR detection of both metallic pipes and high-dielectric plastic pipes for which the permittivity of the pipe exceeds that of the host soil. However, for low-dielectric plastic pipes embedded in a high-dielectric medium, such as an air-filled PVC pipe in wet sand, a full mathematical analysis of the scattering of cylindrical electromagnetic waves indicates that the GPR signature of the pipe is actually stronger in a TE-mode experiment. The reader is referred to Radzevicius and Daniels (2000) for further details.

Since the capability of a GPR experiment to image a buried elongated cylinder depends on the orientation of the TX and RX dipoles relative to the long axis of the target, it is advisable if time and resources permit to acquire data in both the TE- and TM-mode configurations. A third configuration, crossed-dipoles, in which the TX and RX dipole axes are perpendicular, can also be used profitably to image depolarizing subsurface targets. In fact, Sassen and Everett (2009) describe a *polarimetric* GPR technique for imaging subsurface fractures of unknown orientation. In this technique, data from all three configurations (TE, TM, and crossed-dipoles) are acquired over a 2-D survey grid and, at each measurement point, they are assembled into a 2×2 scattering matrix. The scattering matrix is then rotated to determine which TX–RX dipole alignment would have generated the strongest coupling to the target. The rotation angle determines the strike of the target while the largest eigenvalue of the scattering matrix provides the strength of the coupling.

9.14 GPR guided waves

Near-surface guided waves can be established using ground-penetrating radar if the ground contains a low-velocity layer whose thickness is comparable to an electromagnetic wavelength (Strobbia and Cassiani, 2007; van der Kruk *et al*., 2009). The analysis of guided waves in such layers can reveal information about soil moisture conditions or the presence of contaminants. In a typical situation, a wet soil layer resides beneath the high-velocity air layer ($v = c = 0.3$ m/ns) and above an impermeable bedrock. A soil layer in the vadose zone, by virtue of its high water content, generally has a low velocity. Other situations in which guided waves might be set up include a permafrost layer or a wet-soil horizon overlying dry sand or gravel.

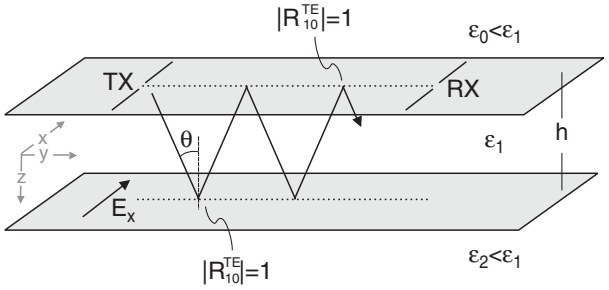

Figure 9.30 TE-mode excitation of a low-velocity GPR waveguide. After van der Kruk *et al*. (2009).

In guided-wave energization, a significant fraction of the transmitted signal from the GPR antenna propagates horizontally at low attenuation within the low-velocity layer. Guided waves are dispersive, that is, the propagation velocity is a function of frequency. Low-frequency components appear to propagate faster than higher-frequency components with the result that the transmitted pulse broadens and becomes distorted with increasing source–receiver separation. Guided waves can dominate GPR reflections and refractions and hence complicate the interpretation of data acquired in the WARR, or variable-offset, mode.

Consider a simple planar waveguide formed by a low-velocity layer $v_1 = c/\sqrt{\varepsilon_1}$ of thickness h, surrounded by two higher-velocity layers $v_0 = c/\sqrt{\varepsilon_0}$ and $v_2 = c/\sqrt{\varepsilon_2}$. For convenience, the GPR antennas are assumed to be oriented as shown in Figure 9.30, such that the TE mode is energized. A TM-mode waveguiding effect is also possible but not discussed here.

As shown in the figure, a wave incident on the lower (v_1, v_2) interface at an angle θ greater than the Snell critical angle is totally reflected so that $|R_{12}^{TE}| = 1$. Similar remarks apply to a wave incident on the upper (v_0, v_1) interface, such that $|R_{10}^{TE}| = 1$. The total internal reflection of this wave is a characteristic feature of ideal waveguiding. Outside the layer in this case, there are only evanescent waves that do not radiate significant energy into the underlying layer (say, bedrock) or overlying layer (say, air). Inside the layer, the total internal reflection implies a greatly reduced attenuation of the horizontally propagating wave. Less efficient, or leaky, waveguides can be formed when the reflection coefficients at the top and bottom are less than unity.

It is shown in Appendix E that a waveguide can support waves propagating in the $\hat{\mathbf{y}}$ direction of the form $E_x \sim \exp[i(k_y y - \omega t)]$. The quantity k_y is the wavenumber in the direction of the wave propagation. However, only certain *modes*, or waves with certain combinations (k_y, ω) of frequencies and wavenumbers, can propagate within the waveguide. In particular, from Appendix E, the waveguide modes must satisfy the non-linear constraint equations

$$\alpha_1 h = \tan^{-1}\left(\frac{\alpha_2}{\alpha_1}\right) + \tan^{-1}\left(\frac{\alpha_0}{\alpha_1}\right) + m\pi; \quad m = 0, 2, 4, \ldots \quad \text{(even)} \tag{9.49}$$

where $\alpha_i = \mu_0 \varepsilon_i \omega^2 - k_y^2$.

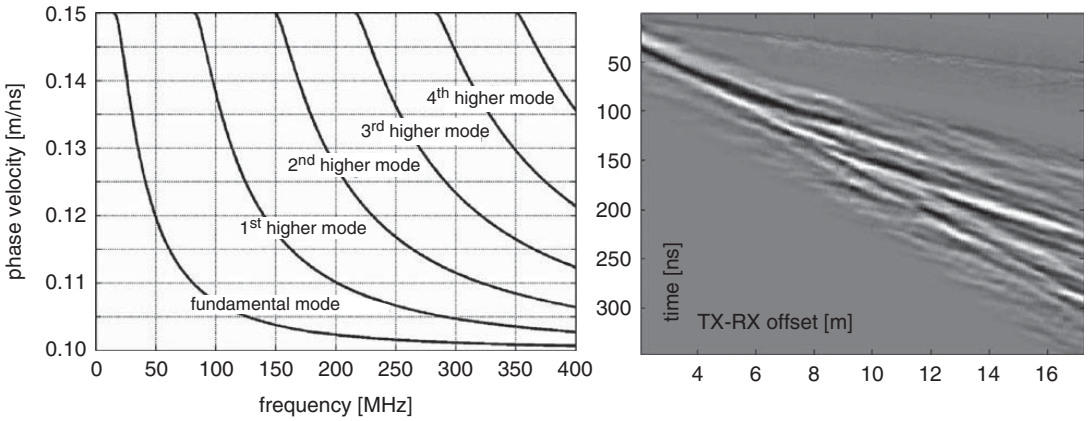

Figure 9.31 (Left) Fundamental mode and first five higher modes in a simple asymmetric waveguide. (Right) Radargram with strongly dispersive guided waves. After Strobbia and Cassiani (2007).

The value $m = 0$ corresponds to the first waveguide mode, the value $m = 2$ represents the first higher mode; $m = 4$ is the second higher mode, and so forth. For each mode m, Equation (9.49) can be viewed as an implicit equation $f(k_y, \omega) = 0$ in the two variables k_y and ω, assuming a waveguide of fixed thickness h and dielectric constants ε_0, ε_1, ε_2. In other words, Equation (9.49) represents, for each mode m, a *non-linear constraint* on the horizontal wavenumber and frequency. For a given frequency ω, the allowed wavenumbers k_y are those that make $f(k_y, \omega)$ vanish. In this way, a *dispersion relation* $k_y(\omega)$ is constructed. Define the waveguide *phase velocity* to be $v(\omega) = \omega/k_y(\omega)$. The phase velocity is a measure of the apparent velocity, within the waveguide, of signals of a given frequency.

An example of the waveguiding effect with $h = 1.0$ m is shown in Figure 9.31, left. Notice that the waveguide signal propagation velocity varies between that of the bedrock (in this case $v_2 = 0.15$ m/ns), at low frequency, to that of the soil ($v_1 = 0.1$ m/ns) at higher frequencies. The fundamental ($m = 0$) mode carries most of the guided energy. Notice that the higher waveguide modes exist only above a certain *cut-off frequency* that depends on m. The dispersive nature of guided waves, that is $v = v(\omega)$, implies that the radar signals spread out with increasing distance traveled along the waveguide; the behavior known as *shingling* is shown in Figure 9.31, right, and it is an effect that is often seen in practical radargrams. Notice that the individual waveguide modes are not easy to identify in the radar image.

Further insight into GPR guided-wave behavior is provided by van der Kruk *et al*. (2009) using the FDTD forward-modeling approach. In Figure 9.32 snapshots are shown of the electric field $E_x(y, z)$ due to transient pulse excitation of a surface waveguide structure. The snapshots reveal trapped electromagnetic energy inside the waveguide and two TE modes can be identified. A leading TE_0 mode has a single-peak amplitude over the vertical range of the waveguide, while a trailing TE_1 mode has a more complicated bimodal signature with alternating positive (red) and negative (blue) peak amplitudes.

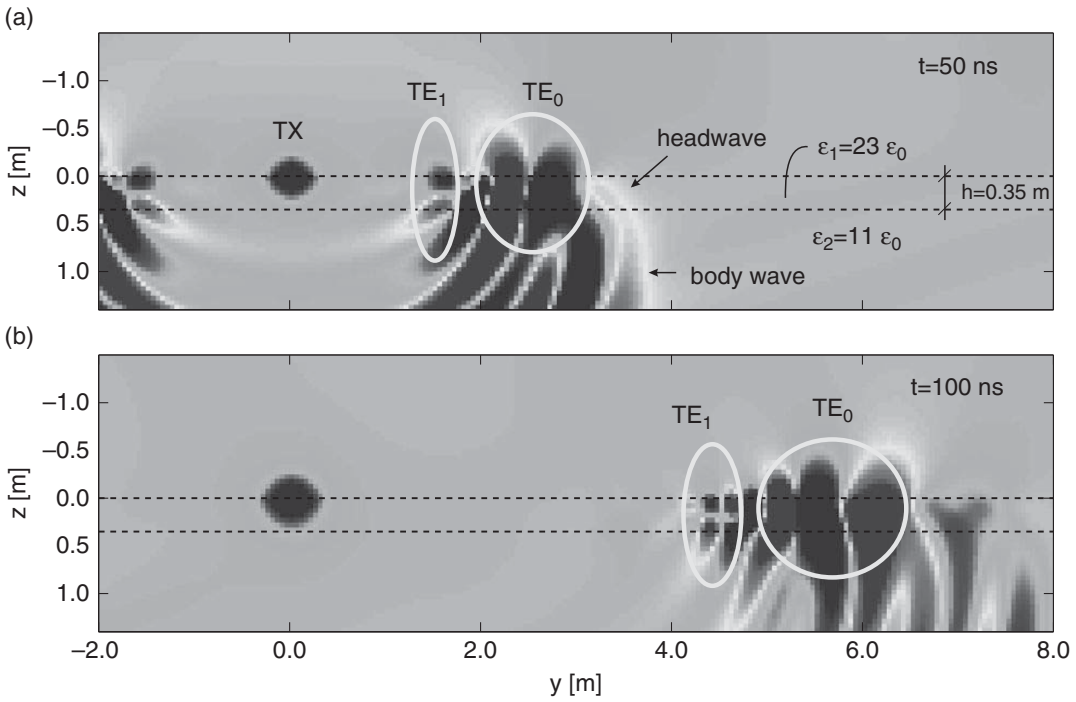

Figure 9.32 Simulations of the electric field E_x within a surface waveguide structure at times (a) $t = 50$ ns and (b) $t = 100$ ns after a pulse is transmitted from the transmitter (TX). The lowest two TE waveguide modes are identified. After van der Kruk *et al*. (2009).

9.15 GPR illustrative case histories

Example. Coastal sedimentology.

Ground-penetrating radar has been widely used in sedimentology (Neal, 2004), a discipline that has long relied on seismic sequence stratigraphy as the primary interpretive tool. GPR interpretation is based on identifying radar surfaces and radar facies contained within the sections, combined with ground truth obtained from traditional geological information such as aerial photographs, outcrops, cores, and trenches. The basic assumption underlying a successful GPR interpretation is that bedding structures which cause reflections can be recognized in radar sections and that non-geological reflections are readily identified and either ignored or removed via data processing. As in the seismic techniques, the knowledge and experience of the GPR interpreter remains key to making accurate and reliable sedimentological inferences. There are many potential pitfalls in the data-acquisition, processing, and interpretation stages of both techniques.

In a recent sedimentological application, GPR was used successfully on the Florida Gulf Coast barrier islands to characterize the depth and lateral extents of erosional surfaces and washover deposits associated with hurricane landfalls (Wang and Horwitz, 2007). The interpreted water table is shown in Figure 9.33, as is the base upon which the 2004

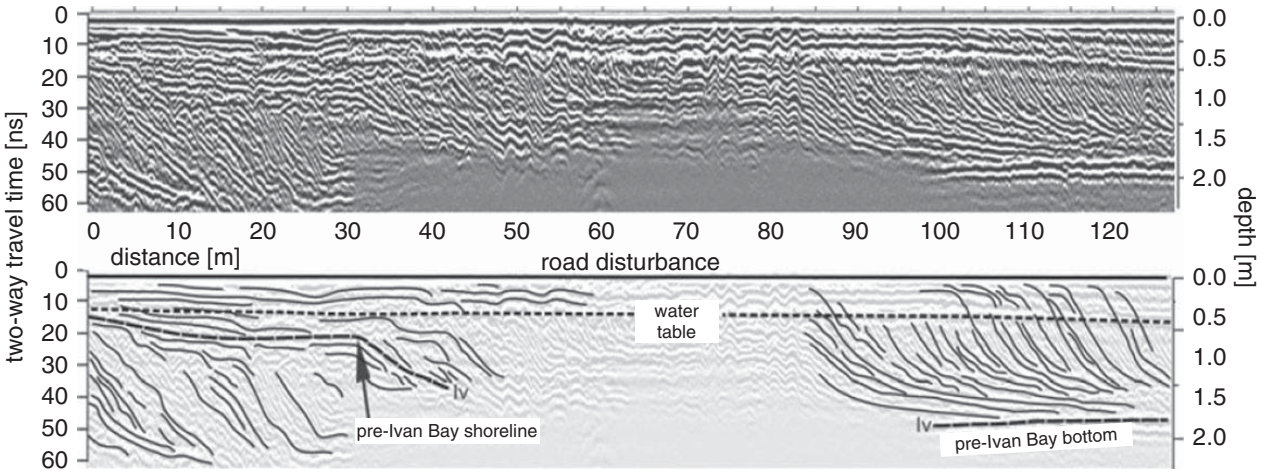

Figure 9.33 (a) 250 MHz radar transect from Florida Gulf coast barrier islands; (b) stratigraphic interpretation; Iv = radar surface interpreted as the shoreline prior to 2004 Hurricane Ivan. After Wang and Horwitz (2007).

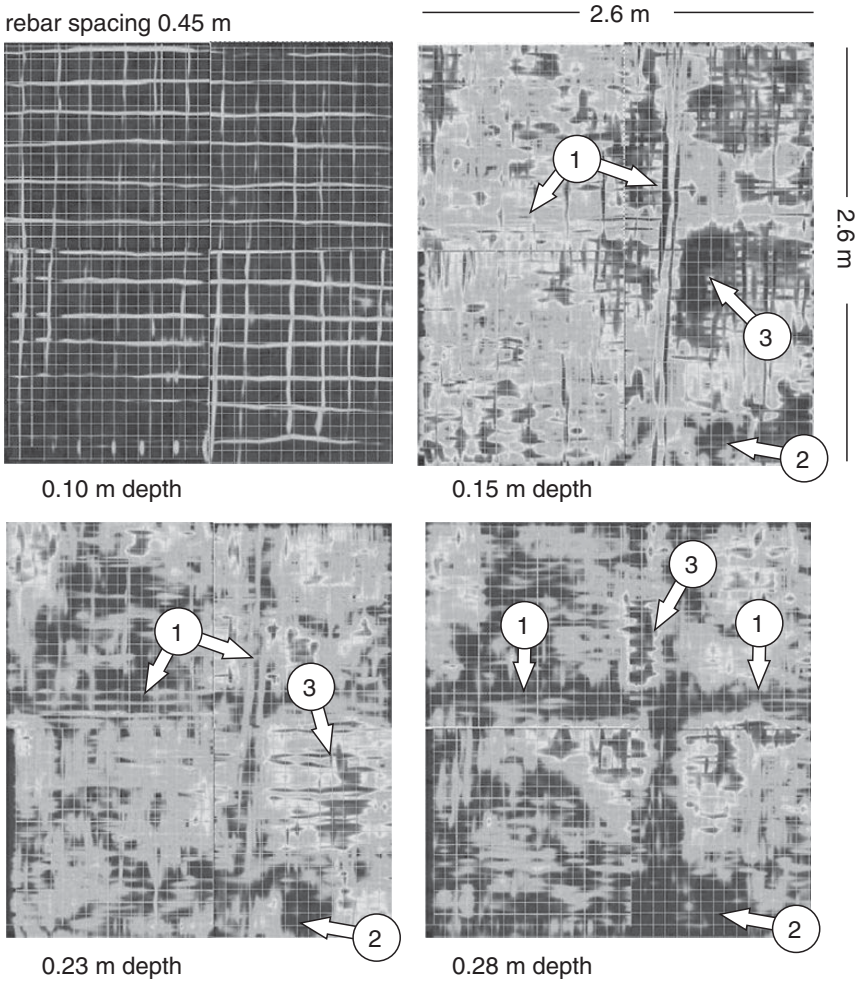

Figure 9.34 1.0 GHz radar depth slices, velocity 0.1 m/s, reinforced concrete floor. 1 = support beam; 2 = support pier; 3 = void space; data courtesy Mary Jo Richardson and Wilf Gardner.

Hurricane Ivan washover was deposited. The GPR data proved in this case to be useful in characterizing coastal geomorphological alterations and shoreline-shaping processes that accompany large storms.

Example. Voids beneath reinforced concrete.

In 2006, a residential garage in central Texas built on expansive clay soil shifted ~ 3.8 cm during an extended dry period. A foundation engineer tried to stabilize the garage floor by raising it, installing piers around its perimeter, and injecting grout into the newly created void spaces. Months later, rainfall was observed to infiltrate beneath the raised concrete floor suggesting that the void spaces had not been adequately filled. Further shifting of ~ 2.0 cm occurred over the next three years. A 1.0 GHz GPR survey of the floor with ~ 15-cm station and ~ 15-cm line spacing was then conducted with an objective to determine the extent of the voids. The resulting series of depth slices shown in Figure 9.34 clearly reveals the rebar grid, the original concrete support beams, a support pier installed by the engineer, in addition to a number of putative void spaces. The latter were subsequently confirmed by drilling. The identified void spaces were then filled with pressurized grout in a second attempt at stabilizing the garage floor. This successful case history demonstrates how GPR data were used to guide a small-scale geotechnical remediation project.

Problems

1. Show that electric field **E** and the magnetic field **B** for lossless plane-wave propagation are linked by $B = (k/\omega)\,\hat{\mathbf{z}} \times E$ and hence the three vectors **E**, **B**, and $\hat{\mathbf{z}}$ (the direction of propagation) are mutually orthogonal.
2. Show that the real and imaginary parts of the complex wavenumber $k = \sqrt{\omega^2\mu\varepsilon + i\omega\mu\sigma}$ are given by Equations (9.24) and (9.25).
3. Show that the phase difference between the electric field **E** and the magnetic field **B** is Ω where $\tan\Omega = \sqrt{1+Q^2} - Q$, and $Q = \omega\varepsilon/\sigma$. Does **E** lead or lag **B** when the plane wave is viewed as a function of position, for a fixed instant of time? What about the case when the plane wave is viewed as a function of position?
4. Consider a vertically polarized (TM-mode) plane wave obliquely incident on the planar interface separating two lossless dielectric media. The electric-field vector **E** is parallel to the plane of incidence and orthogonal to the propagation direction $\hat{\mathbf{p}}$. The magnetic-field vector **H** is perpendicular to the plane of incidence and parallel to the interface. Show that the reflection coefficient in this case is given by